JGR Oceans

RESEARCH ARTICLE
10.1029/2021JC017865

Mechanisms for Late 20th and Early 21st Century Decadal AMOC Variability

Alex Megann[1], Adam Blaker[1], Simon Josey[1], Adrian New[1], and Bablu Sinha[1]

[1]National Oceanography Centre, Southampton, UK

Key Points:

- We use three 1/4° forced NEMO integrations to investigate mechanisms for AMOC variability
- Decadal AMOC variability is mainly forced by winter cooling in the Irminger Sea, and to a lesser extent by cooling in the Labrador Sea
- An annual index, derived from the surface-forced stream function and accumulated over 10 years, has predictive skill for the AMOC strength

Correspondence to:

A. Megann,
apm@noc.ac.uk

Citation:

Megann, A., Blaker, A., Josey, S., New, A., & Sinha, B. (2021). Mechanisms for late 20th and early 21st century decadal AMOC variability. *Journal of Geophysical Research: Oceans*, *126*, e2021JC017865. https://doi.org/10.1029/2021JC017865

Received 26 AUG 2021
Accepted 24 NOV 2021

Author Contributions:

Conceptualization: Adrian New
Investigation: Bablu Sinha
Methodology: Bablu Sinha
Resources: Bablu Sinha
Software: Bablu Sinha
Writing – review & editing: Adrian New, Bablu Sinha

Abstract Recent studies using data from the OSNAP observational campaign and from numerical ocean models suggest that the Iceland Basin and the Irminger Sea may be more significant for formation of upper North Atlantic Deep Water than the Labrador Sea. Here, we present a set of hindcast integrations of a global 1/4° NEMO simulation from 1958 until nearly the present day, forced with three standard forcing data sets. We use the surface-forced stream function, estimated from surface buoyancy fluxes, along with the overturning stream function, similarly defined in potential density space, to investigate the causal link between surface forcing and decadal variability in the strength of the Atlantic meridional overturning circulation (AMOC). We use the stream functions to demonstrate that watermasses in the simulations are transformed to higher densities as they propagate around the subpolar gyre from their formation locations in the north-east Atlantic and the Irminger Sea, consistent with the picture emerging from observations. The surface heat loss from the Irminger Sea is confirmed to be the dominant mechanism for decadal AMOC variability, with the heat loss anomaly from the Labrador Sea having about half the magnitude. A scalar metric based on the surface-forced stream function, accumulated in time, is found to be a good predictor of changes in the overturning strength. The AMOC variability is shown to be related to that of the North Atlantic Oscillation (NAO), primarily through the surface heat flux, itself dominated by the air-sea temperature difference, but also with some local feedback from the SST to the surface fluxes.

Plain Language Summary The Atlantic Meridional Overturning Circulation (AMOC), which brings warm waters to the North Atlantic and warms the climate of northern Europe, is known to vary on time scales from annual to many centuries, with significant impacts on European climate. In this paper, we use three numerical model integrations, linking decadal-time scale changes in the rate of formation of the deep waters exported southwards to changes in the sea surface fields used to force the models. We show that AMOC variability is linked most strongly to wintertime cooling over the Irminger Sea, with cooling over the Labrador Sea having a smaller influence. Using the rates of density increase at each latitude due to surface cooling, accumulated over 10 years, we create an annual index that follows the AMOC strength closely, and show that this has the potential to predict AMOC changes.

1. Introduction

The projections of the models included in the Coupled Model Intercomparison Project Phase 5 (CMIP5) indicate a reduction in the strength of the Atlantic meridional overturning circulation (AMOC) into the 21st century as a result of anthropogenic greenhouse gas emissions (Cheng et al., 2013), leading to a substantial cooling over northern Europe resulting from the associated reduction in ocean heat transport (Liu et al., 2020). At the same time, variations occur on time scales from interannual to decadal, and these too have at least as strong an influence on European climate as the longer-term trends. In particular, AMOC variations are linked to multidecadal swings in the North Atlantic Sea surface temperature index, the Atlantic Multidecadal Variability (AMV), with known impacts on the weather and climate (including temperature, rainfall, and hurricane activity) of the adjacent continents and further afield (see e.g., Sutton et al., 2018). Recent reports of an apparent decline in the AMOC have created more than a little interest, with a reduction of about 3 Sv at 26°N since 2008 being reported in the RAPID time series (Smeed et al., 2018), which is significantly more rapid than the projected decrease from increasing CO_2 concentrations. To place this variation in the context of longer time scales, estimates of the AMOC strength based on proxy data such as temperature and surface elevation have been used to extrapolate the AMOC strength before the RAPID era: Worthington et al. (2020) used the 26°N RAPID data to create an empirical model which they then applied to earlier hydrographic data sets, deriving an AMOC time series that has a maximum in the late 1990s, followed by a gradual reduction toward the start of the RAPID campaign in around 2005. Further

back, less robust proxy data (e.g., Delworth et al., 2016) suggest that the AMOC gradually rose from the 1970s to the peak in the 1990s. There have been recent suggestions that the AMOC is currently in a recovery phase after the decline reported by Smeed et al. (2018) and others. The overturning and surface-forced indices derived by Desbruyères et al. (2019) at 45°N from observational data sets show a decline of about 3 Sv from 1993 to 2010, followed by a sharp increase of about 4 Sv between 2010 and 2018, and Moat et al. (2020) use data from the RAPID array at to estimate a recovery of a similar magnitude over the same period. Jackson et al. (2019) evaluate the overturning strength at 26°N and at 50°N in a set of ocean reanalyses: at 26°N, these agree quite well with the RAPID observations from 2004 onwards of a downward trend from 2005 and a sharp dip in 2010, followed by a slight increase, while at 50°N, the AMOC in the reanalyses has a slight downward trend from 1995 to 2013, with interannual variation of around +-1 Sv that masks any potential recovery after 2010, which in any case is smaller than the variation.

The downwelling leg of the AMOC in the North Atlantic, driven by episodes of winter buoyancy loss at multiple locations in the subpolar gyre and the Nordic Seas, and leading to the production of southward-flowing North Atlantic Deep Water (NADW), has long been understood as a central control on the strength of the overturning circulation, and thence on the meridional ocean heat transport. Until the last decade, the consensus has been that this system was dominated by convection in the Labrador Sea and the Nordic Seas, with each contributing about half of the total volume of the NADW (e.g., Mauritzen, 1996; Schmitz & McCartney, 1993; Worthington, 1976), and analysis of numerical models (e.g., Bleck & Sun, 2004; Danabasoglu et al., 2012; Eden & Willebrand, 2001; Kuhlbrodt et al., 2007; Roberts et al., 2013), reinforced this view.

Nevertheless, one or two authors questioned this hypothesis; e.g., Pickart et al. (2003) suggested that "Labrador Sea Water," constituting the upper portion of NADW, was in fact mainly created in the Irminger and Iceland Basins, and over the past decade the prevailing consensus has been seriously challenged by the availability of more comprehensive observations (in particular, the Overturning in the Subpolar North Atlantic Programme, OSNAP) and by improved numerical models. Lozier et al. (2019) and Zou and Lozier (2016) used OSNAP data and a numerical model study, respectively, to investigate the strength of the links between variability of the AMOC and variability in the rate of deep water production and export, and conclude that the bulk of watermass conversion and its variability occurs east of Cape Farewell (i.e., in the Irminger Basin), and that the Labrador Sea has a minimal contribution to the total overturning. Other studies have strengthened the argument: Chafik and Rossby (2019) use hydrographic data to estimate transports in density classes, suggesting that the Nordic Seas, rather than the Labrador Sea, are key to the state of the MOC; while Petit et al. (2020) conclude that the lower limb of the AMOC is primarily composed of waters formed in the Nordic Seas and Irminger and Iceland basins.

A number of the foregoing studies have related the variability in production rate of NADW, and hence that of the AMOC, to variability in surface buoyancy fluxes, the latter themselves reflecting climatic indexes, primarily the North Atlantic Oscillation (NAO). The interannual and interdecadal variability in the properties of upper NADW, estimated using up to 60 years of hydrographic data, have been linked to changes in the North Atlantic Oscillation (NAO) index (Curry et al., 1998; Kieke & Yashayaev, 2015; Stramma et al., 2004), with positive phases of the NAO corresponding to periods of stronger NADW production. Josey et al. (2019) ascribed at least some of the interannual variability in Irminger Sea convection to intense cooling events traced to Greenland tip jets, the latter in turn related to the relative strengths of the East Atlantic Pattern (EAP) and the NAO.

The causes of the NAO changes which drive NADW production are still debated. A null hypothesis is that NAO variability is essentially random and internally generated in the atmosphere (e.g., the unforced coupled model study of Dong & Sutton, 2005). However, there are hints in some coupled model studies that suggest a weak feedback from the ocean (Ortega et al., 2017) arising from the AMOC and subsequent subpolar SST response to the NAO. The possibility of oceanic feedbacks contributing to NAO trends is further evidenced by Peings and Magnusdottir (2014) using multidecadal atmospheric reanalysis, observed SST and forced atmosphere simulations. Additionally, a number of studies have argued that external forcing may force the NAO and hence the AMOC. Öttera et al. (2010) provide evidence that solar and volcanic forcing may influence NAO trends, while Menary, Jackson, and Lozier (2020) and Menary, Robson, et al. (2020) highlight the sensitivity of the AMOC to the balance between anthropogenic aerosol and greenhouse gas forcing. The mechanism whereby aerosol forcing impacts the AMOC is still unclear, but is likely to be related to its influence on atmospheric circulation (including the NAO) and turbulent heat air-sea buoyancy fluxes rather than a direct impact on incident shortwave radiation (e.g., Robson et al., 2016). The attribution of NAO variability to external drivers and/or internal variability is

further confounded by the "signal to noise problem" in climate models, which operates at least up to decadal time scales and possibly longer (Smith et al., 2020). For as yet unexplained reasons, climate models underestimate the predictable fraction of the total variability of the NAO by an order of magnitude making it difficult at present to understand the drivers of observed changes in the NAO, such as the increasing trend seen between the 1960s and 1990s.

The representation of the meridional overturning circulation by a stream function in density coordinates, instead of the conventional fixed-depth coordinate, is more faithful to the tendency of watermasses to follow isopycnal surfaces rather than depth levels, and in particular avoids the aliasing of the gyre circulation onto the overturning (e.g., Sidorenko et al., 2021; Sun & Bleck, 2001; Xu et al., 2018). With an appropriate choice of the density coordinate, and with the restriction that it only presents a zonally averaged picture, the use of a density representation of the AMOC allows near-adiabatic large-scale flow along isopycnals to be distinguished from diapycnal flow, and the rate of diabatic density transformation (resulting from a combination of the physical, and, in the case of models, numerical contributions to mixing, and processes associated with the nonlinear equation of state) may be estimated from the divergence of the flowlines (e.g., Lee et al., 2002; Megann, 2018). Nevertheless, the overturning stream function represents transformations resulting both from internal processes and from surface buoyancy fluxes, and cannot be used directly to distinguish between them. Sidorenko et al. (2020, 2021) analyzed the AMOC in density space in the FESOM ocean model and in the AWI coupled climate mode, respectively, and in addition used estimates of the diapycnal transports through two-dimensional density surfaces, noting a link with the NAO and concluding that dense water formation in the eastern side of the North Atlantic was substantially stronger than in the Labrador Sea.

The surface-forced stream function analysis (e.g., Marsh, 2000) is based on the watermass transformation framework of Walin (1982) and of Speer and Tziperman (1992), and relates the rate of density transformation in a given latitude and density class to the surface buoyancy fluxes into that density class over its outcrop area. In a steady state, and in the absence of mixing processes, cabbeling and thermobaricity, the surface-forced stream function Ψ_{surf}, at a given latitude and density, would converge to Ψ, the time-averaged overturning stream function. In the real world, Ψ_{surf} evaluated from monthly surface fields as an annual mean has been found to be a good approximation to Ψ, with the caveat that the overturning at a given latitude results from an accumulation of the buoyancy fluxes over a period of between 5 and 10 years, with longer lags generally observed at lower latitudes. So, in principle, at least, the difference between the overturning and surface-forced stream functions can be interpreted as representing the internal transformations (e.g., Sidorenko et al., 2020). This technique has been applied to a range of data sets including reanalyses (Grist et al., 2014; Josey et al., 2009), forced ocean models (Grist et al., 2012; Kostov et al., 2019); coupled climate models (Josey et al., 2009) and hydrographic data (Desbruyères et al., 2019). All of these studies have confirmed that there is a significant level of correlation between the strength of the surface-forced stream function and that of the overturning stream function, with an appropriate lag applied: Josey et al. (2009) used a combination of the HadCM3 coupled model and the NCAR reanalysis, and found that the lag between surface forcing and the overturning increased equatorward from 6 years at 65°N to 15 years at 36°N. Desbruyères et al. (2019) estimated Ψ_{surf} using observational SST and SSS and surface fluxes from the NCEP2, ERA-I, and CERES climatologies, defining annual indices from the maximum values of the respective stream function, and again found significant lagged correlations between surface-forced stream functions and observed estimates of AMOC strength at 45°N. Kostov et al. (2019) investigated the sensitivity of the AMOC strength to variations in the surface fluxes over the seasonal cycle, and found delays of between 8 and 80 months, depending on the season in which the flux anomalies occur.

Motivated by the OSNAP results, and by the increasing emphasis on the eastern subpolar gyre (SPG) as an important water mass transformation region (e.g., Petit et al., 2020), we investigate regional contributions (the Labrador Sea, the Irminger Sea, the eastern subpolar North Atlantic, and the Nordic Seas) to the surface-forced stream functions in order to pinpoint the most important areas. We further investigate how prevailing atmospheric conditions influence the air-sea buoyancy fluxes in these regions, along with the impact of ocean circulation-related SST feedbacks, as these aspects have not been addressed by previous studies. In this paper, we use a set of three hindcast integrations of a global 1/4° NEMO ocean configuration, with a selection of standard surface forcing data sets, and use the surface-forced stream function technique to relate the regional variability of surface fluxes to watermass formation, and thence to the variability of the strength of the meridional overturning.

Table 1
Integration Period and Forcing Frequencies Used for Model Integrations

Forcing set	Integration	Wind speed	Radiation	SAT, humidity	Precipitation
CORE2	1958–2007	Six-hourly	Daily	Six-hourly	Monthly
DFS5.2	1958–2015	Three-hourly	Daily	Six-hourly	Daily
JRA-55	1958–2020	Three-hourly	Three-hourly	Three-hourly	Three-hourly

In Section 2, we describe the model configuration and the experimental design, and in Section 3, we introduce the methodology and analysis. In Section 4, we describe the decadal evolution of the AMOC in the simulations, using the surface-forced stream function framework to relate this to changes in the surface buoyancy loss. We demonstrate that the decadal-time scale variability is caused mainly by variability in the wintertime heat loss, primarily in the Irminger Sea, and discuss the local causes of heat flux variability, relating the latter to principal North Atlantic climatic indices. In Section 5, we summarize our results and discuss their significance.

2. Model Description

The model is the GO6 configuration (Storkey et al., 2018), consisting of version 3.6 of the NEMO ocean model (Madec & the NEMO team, 2017), and the GSI8.1 configuration of the Los Alamos National Laboratory sea-ice model, CICE (Hunke & Lipscomb, 2010; Ridley et al., 2018). The latter consists of version 5.1.2 of the CICE base code with multilayer, energy-conserving thermodynamics (Bitz & Lipscomb, 1999), elastic-viscous-plastic ice rheology (Hunke & Dukowicz, 1997) and multicategory ice thickness (Bitz et al., 2001) with five thickness categories. Details of the availability of the code are in Appendix A. The grid is the eORCA025 global 1/4° grid. Ice shelf cavities are closed, and the freshwater fluxes under the ice shelf are prescribed.

The vertical mixing parameterization scheme is a modified version of the Gaspar et al. (1990) turbulent kinetic energy (TKE) scheme (Madec & the NEMO team, 2017). The Lagrangian iceberg model of Bigg et al. (1997) and Martin and Adcroft (2010), which was implemented in NEMO by Marsh et al. (2015) is used.

2.1. Initialization and Forcing of Model Integrations

The simulations were all initialized at rest from a climatology based on a mean of years 2004–2008 of the EN3 climatology (Ingleby & Huddleston, 2007. Three data sets (see Table 1) are used to force the ocean integrations: CORE2 (Large & Yeager, 2009), DFS5.2 (Dussin et al., 2016), JRA55-do v1.3 (Tsujino et al., 2018), with the latter updated to JRA55-do v1.5 for the last six years.

The JRA55 integration was forced with a combined precipitation field (as required for NEMO v3.6) that was constructed from the rainfall and snowfall fields from the JRA55 data set.

Table 2
Regions for Integration of Surface Fluxes

Basin	Zonal limits	Meridional limits
Labrador Sea	47°–65°N	70°–40°W
Irminger Basin	47°–65°N	40°–20°W
North-east Atlantic	47°–65°N	20°–0°W
Nordic Seas	65°–85°N	20°W–20°E

3. Analysis Methodology

We define the buoyancy flux per unit area F_ρ (e.g., Schmitt et al., 1989) as

$$F_\rho = -\rho\left(\alpha\frac{Q_H}{\rho C_P} - \beta\frac{S\ Q_{FW}}{1-S}\right) \quad (1)$$

where α and β are the thermal expansion and haline compressibility, respectively; S is the salinity, ρ is a reference density equal to 1,026 kg m^{-3}, Q_H is the net downward heat flux per unit area; Q_{FW} is the net freshwater volume flux per unit area into the ocean, including iceberg melting and river runoff; and C_p is the specific heat capacity, set here to 3,990 J kg^{-1} K^{-1}. F_ρ has the dimensions of kg m^{-2} s^{-1}.

We define the regions we shall use for analysis in Table 2 (these are also illustrated in Figure 2). Although we shall mainly present results for area-integrated fluxes, we note that the ocean areas of these regions are quite comparable: the Nordic Seas at 2.0×10^6 km^2 is the smallest, and the Labrador Sea at 2.5×10^6 km^2 is the largest.

The surface-forced stream function $\Psi_{surf}(\rho,\Theta)$ (Marsh, 2000, and elaborated by Grist et al., 2009) expresses the rate of density transformation by surface buoyancy fluxes at latitude Θ

$$\Psi_{surf}(\rho,\Theta) = \frac{(D(\rho,\Theta) - D(\rho+\Delta\rho,\Theta))}{\Delta\rho} \quad (2)$$

where $D(\rho,\Theta)$ is the area integral of the surface buoyancy flux F_ρ, as defined in Equation 1, into the surface density range $(\rho, \rho+\Delta\rho)$, evaluated from the most northerly surface outcrop of the isopycnal ρ to some fixed northern boundary, and we assume a steady state. Because the rows of the eORCA025 grid are not parallel to lines of constant latitude at high northern latitudes, the integrals were carried out on grid rows, rather than lines of given latitude, and the northern boundary was defined as a constant j-index: this was set to $j = 1{,}100$, corresponding in the North Atlantic domain discussed here to latitudes between 75°N and 78°N. In the results presented here, annual means of $\Psi_{surf}(\rho,\Theta)$ are evaluated from monthly mean model fields; although this averaging time will miss dense water formation events on shorter time scales, it was the highest frequency available, and errors in general are unlikely to be large (see e.g., Marsh, 2000), although—as we note in Section 4.2—the rarity of ventilation of the very densest waters may lead to significant inaccuracies for these density classes. If transformation rates due to interior mixing processes and the effects of nonlinearity of the equation of state are relatively small compared with the those of the surface transformations, and if we can neglect changes in isopycnal volume on annual time scales, $\Psi_{surf}(\rho,\Theta)$ will be a good approximation to the full overturning stream function in density classes $\Psi(\rho,\Theta)$, with a lag corresponding to some propagation time at a given latitude Θ, which we shall investigate in Section 4.3. Here, we define the density as σ_2, the potential density with reference to 2,000 dbar pressure, and this is evaluated in 72 density classes, spanning the range $30.0 < \sigma_2 < 37.2$ kg m^{-3}: a linear density scale with spacing 0.5555 kg m^{-3} was used for the density classes for $\sigma_2 < 35.0$ kg m^{-3}, while a logarithmic mapping was used at densities higher than 35.0 kg m^{-3} in order to have an acceptable representation of deep and bottom waters.

The annual overturning stream function $\Psi(\rho,\Theta)$, evaluated from monthly mean velocities mapped onto intervals of the monthly mean density, is generally quite smooth in time, allowing the overturning strength to be usefully characterized by a maximum value in a given latitude and depth or density range. By contrast, the annual surface-forced stream function has been found (e.g., Desbruyères et al., 2019; Grist et al., 2009) to be rather noisy, both in density and in time, rendering the use of single maxima less helpful. We therefore define indices $T_{OV}(t)$ and $T_{SF}(t)$ for the mean overturning and surface-forced stream functions, respectively, as functions of time, by evaluating the mean of the respective stream function over a region of density and latitude space which reliably contains the maxima of the annual mean stream function (allowing for more than one maximum). For the present study, we use the fixed latitude band 48°–58°N and the density range $36.55 < \sigma_2 < 36.95$ (corresponding to a depth range between about 900 and 2,000 m), which contains the maxima of the stream function in almost all years. We find that the overturning stream function has reached a near-equilibrium after the first 15 years; since the data used to generate the forcing fields are sparse before the 1970s anyway, we treat this as a spin-up period. We subtract the mean value over the period from 1976 until the end of the respective integration to give an anomaly time series.

4. Results

4.1. Overturning Strength

Figure 1 shows time series of the overturning strength, defined as the maximum of the Atlantic overturning stream function in the depth range 900–1,100 m, at latitudes 26°N and 45°N, evaluated from the annual mean velocity field, and in the lower two panels the anomalies with respect to the means at each section from 1976 to the end of the respective integration. The AMOC at 26°N from the RAPID array after 2004 (Smeed et al., 2018) is overlain (cyan lines) onto the simulated AMOC strength for 26°N. It can be seen that the overturning strength in the experiments forced by the CORE2 (black) and DFS5.2 (red) is rather similar at both latitudes, but that in the JRA55-forced experiment (green) is consistently 3–4 Sv weaker. The interannual variability of the AMOC

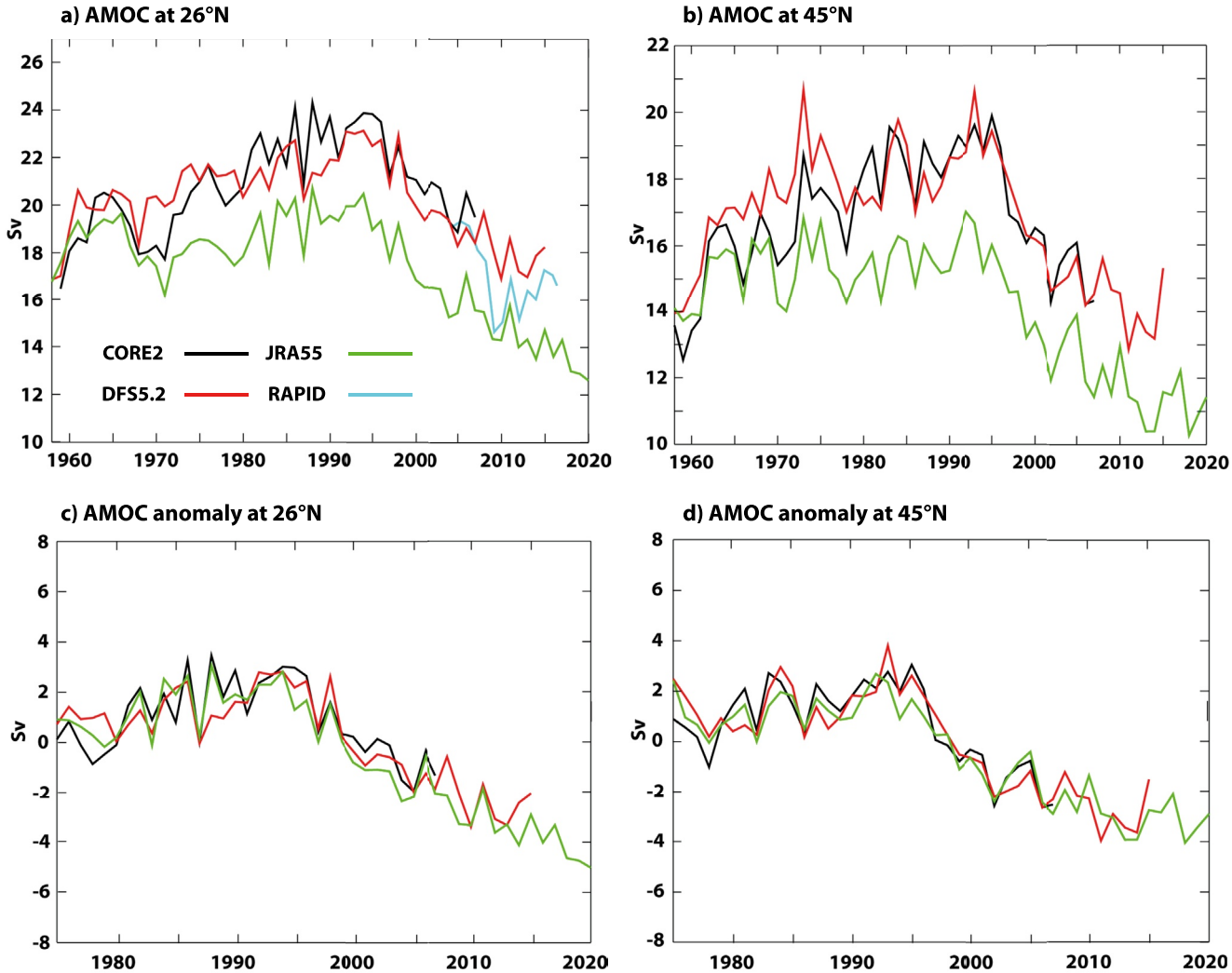

Figure 1. Annual mean Atlantic meridional overturning circulation (AMOC) strength at (a) 26°N and at (b) 45°N over the complete model integrations, and the anomaly from the mean (evaluated from 1976 until the end of each integration) at (c) 26°N and at (d) 45°N. The cyan curve in panel (a) is the annual mean (January-December) transport estimated from the RAPID array (Smeed et al., 2018).

at 45°N is more closely synchronized between the three integrations than it is at 26°N, suggesting that internal, possibly stochastic, processes are more important at the more southerly latitude. The observed AMOC strength at 26°N is intermediate between those in the experiments forced with DFS5.2 and with JRA55.

The CORE2-forced GO6 1/4° configuration described by Storkey et al. (2018) spun up from initialization in 1976 to an unrealistically high AMOC strength at 26°N of over 24 Sv in the 1980s and 1990s, and the CORE2 simulation described here (the black curve in Figure 1a) follows a similar trajectory from its start in 1958, albeit with a slower rate of initial strengthening. The reasons for the rise in strength and for the unrealistically strong AMOC over the first decade or two are not yet fully understood. The simulation described here forced with DFS5.2 (red curve in Figure 1a) closely follows the CORE2-forced simulation, while the JRA-55 simulation by contrast has a much-reduced spin-up transient and, as noted earlier, has a weaker AMOC after this period.

The AMOC anomaly time series (lower panels of Figure 1; note the change in the horizontal axis between the upper and lower panels) shows that the evolution of the AMOC on interannual-to-decadal time scales in the simulations, after the first 18 years of spin-up, is much more consistent between the three integrations once the long-term mean is subtracted. The decadal-time scale evolution over this period is qualitatively consistent with an AMOC index estimated at 50°N from proxy data by Delworth et al. (2016): the latter index rises similarly from the mid-1970s to a maximum in the early 1990s, declining thereafter until about 2010. The decadal-time

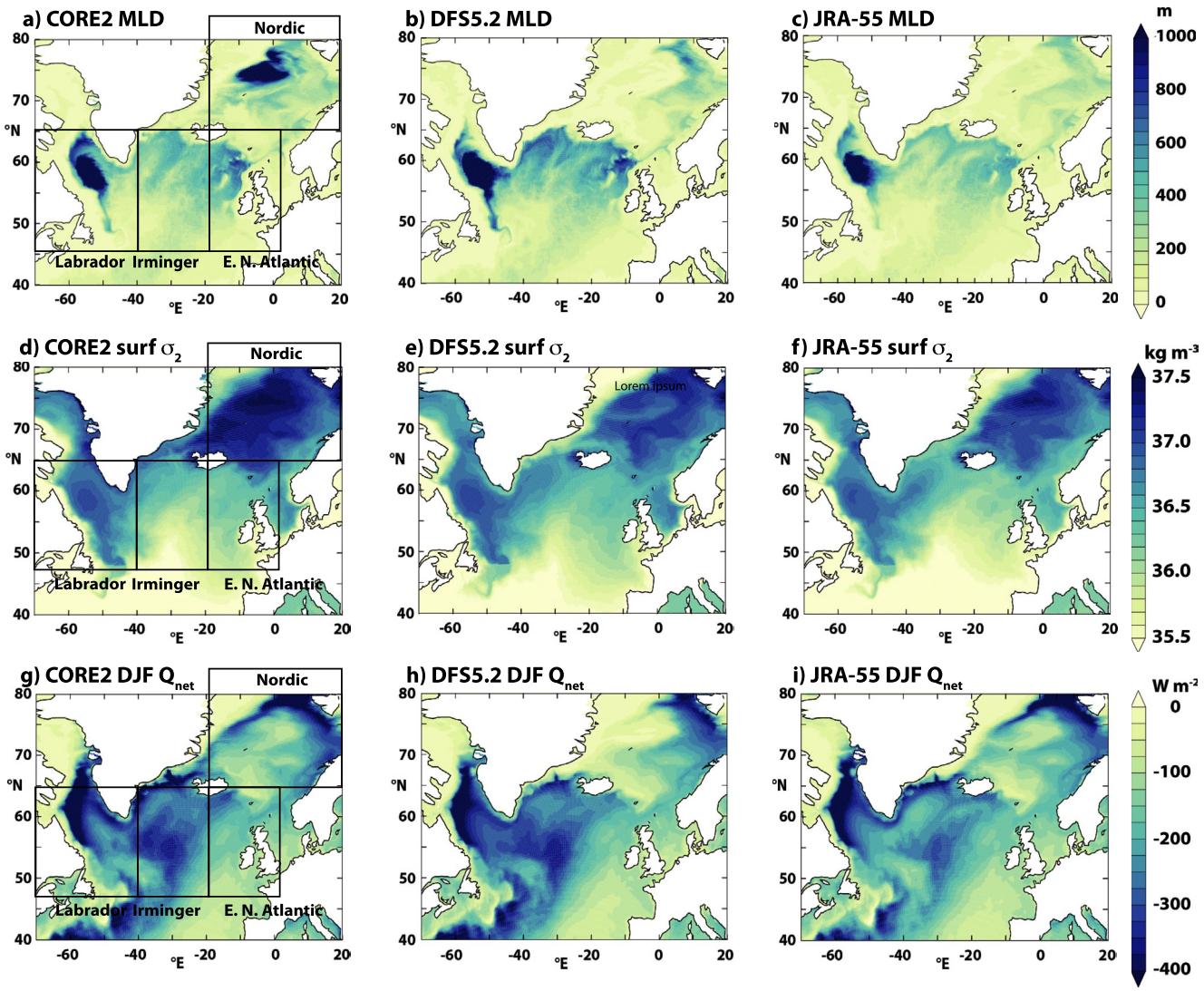

Figure 2. Mean March mixed-layer depth (in m) with (a) CORE2; (b) with DFS5.2; and (c) with JRA-55; and maximum surface potential density σ_2 (in kg m^{-3}) with (d) CORE2; (e) with DFS5.2; and (f) with JRA-55; and mean winter downward heat flux in W m^{-2} with (g) CORE2; (h) with DFS5.2; and (i) with JRA-55. The boxes in the left-hand panels show the regions for analysis defined in Table 2.

scale reduction of about 4 Sv from 1980 to 2010 seen in our simulations are consistent with that estimated by Desbruyeres et al. (2019), but larger than those evaluated by Jackson et al. (2019) from ocean reanalyses, which are dominated by interannual variability with little significant decadal trend. We note that the ensemble mean AMOC in the CMIP6 models (Figure TS11 from Arias et al., 2021) has a prominent peak in the 1980s, whereas the variability in the CMIP5 ensemble (Figure 2a from Cheng et al., 2013) is much weaker. However, neither of the multimodel ensembles match the magnitude of the decadal/multidecadal AMOC variability in our forced simulations, even if a few individual ensemble members for CMIP5/6 might do so.

Figure 2 shows the mean March mixed-layer depth (defined as the depth at which the density is 0.010 kg m^{-3} higher than that at 10-m depth) projected onto a latitude-longitude grid in the North Atlantic in the three experiments (Figures 2a–2c), and the maximum values of the surface potential density σ_2 in each year (Figures 2d–2f), all averaged here over the decade 1996–2005, the latter period chosen for consistency with the analysis in Storkey et al. (2018). The boundaries of the four regions used in our analysis are shown as rectangles superposed onto the left-hand panels. In all the simulations, there is winter convection reaching deeper than 500 m in all four regions, and the convection depth in the Labrador Sea exceeds 1,000 m in all three integrations. The integration forced with CORE2 (Figure 2a) can be seen to have much stronger convection in the Nordic Seas than the other

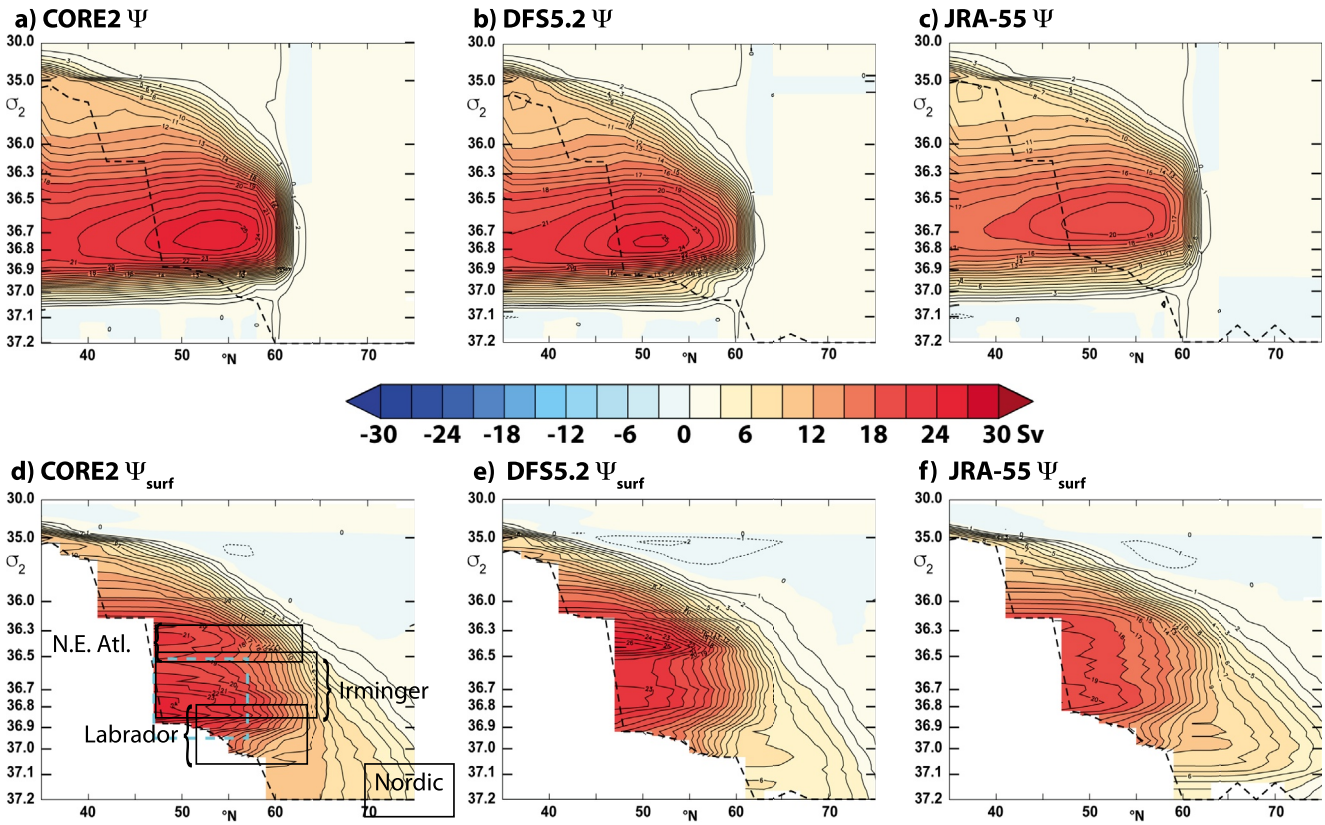

Figure 3. Mean Atlantic meridional overturning stream function in 1996–2005 in experiments forced with CORE2 (a); DFS5.2 (b); and JRA55 (c); and the surface-forced stream function with CORE2 (d); DFS5.2 (e); and JRA55 (f). The dashed cyan box in panel (d) shows the region in density-latitude space over which the overturning metrics $T_{OV}(t)$ and $T_{SF}(t)$ will be evaluated, and the black boxes enclose the respective regions where deep convection occurs (see Figure 2).

two, with patches of mixing exceeding 1,000 m, while the JRA55-forced experiment (Figure 2c) has shallower convection at all sites, consistent with the weaker overturning seen at both 26°N and 45°N in Figures 1a and 1b. North of 65°N (which we class here as the Nordic Seas), densities above σ_2 = 37.1 kg m^{-3} are ventilated; in the Labrador Sea, deep mixing occurs for densities in the range 36.9–37.1 kg m^{-3}; in the Irminger Sea the range is 36.5–36.9 kg m^{-3}; and in the eastern subpolar Atlantic the ventilation is of densities from 36.3 to 36.6 kg m^{-3}. In the Nordic Seas, the surface density is substantially higher with CORE2 forcing, reaching a maximum of over 37.5 kg m^{-3} in a patch at around 75°N, while in the other two experiments this density is only attained in the far north-east, just south of Svalbard. All three simulations have strong winter heat loss (Figures 2g, 2h, and 2i) from the Labrador and Irminger Sea, and also in the far north of the Nordic Seas and in the north-west corner of the north-east Atlantic box. It is interesting that the locations of strongest heat loss are not necessarily coincident with those of deep mixing; in particular, the strong convection in the Greenland Sea in the CORE2 simulation is considerably to the south-west of the near-boundary heat loss, while the dense water formation in the Labrador Sea is in the center of the basin, where the heat loss is around the boundary. This is consistent with the role proposed for eddies by Chanut et al. (2008), Katsman et al. (2018), and others in transporting cold water toward the center of the Labrador Sea to precondition for convection; Megann and Storkey (2021) showed that, although eddies are not usefully resolved at these latitudes in this model configuration, the low default value of the viscosity allows energetic noise-like features in the velocity field that are likely to replace mesoscale eddies in this role.

4.2. Overturning and Surface-Forced Stream Functions in Density Space

Figure 3 shows the Atlantic overturning (upper panels) and surface-forced stream functions (lower panels) in potential density classes, expressed as functions of σ_2 and averaged over the period 1996–2005. The white areas in the surface-forced stream function panels indicate density classes that are not ventilated at those latitudes.

The cyan dashed box overlain onto Figure 3d encloses the region defined in Section 3 over which we evaluate the indices $T_{OV}(t)$ and $T_{SF}(t)$ for the overturning and surface-forced stream functions; the black boxes on the same panel enclose density and latitude ranges typical of deep convection in each of the four regions denoted in Figure 2a.

The overturning stream functions in potential density space (the upper three panels of Figure 3) reveal a clear overall picture: light waters with densities less than $\sigma_2 = 36.7$ enter the basin from the south, and become progressively densified by surface buoyancy losses as they travel north between 45°N and 65°N. The resulting dense waters, with σ_2 between 36.80 and 37.05 kg m^{-3}, return southwards as North Atlantic Deep Water (NADW). In this latter southward-flowing leg, the upper part ($\sigma_2 < 36.9$ kg m^{-3}) undergoes a gradual reduction in density resulting from a combination of physical and numerical mixing (see Megann, 2018 for an analysis of the latter in a similar NEMO configuration), while the waters denser than $\sigma_2 > 36.9$ kg m^{-3} become yet denser, probably through mixing with the underlying Antarctic Bottom Water (AABW). The overturning cell is weaker in the JRA-55 experiment (Figure 3c) than in the other two, with a maximum of 20 Sv, compared with 24 Sv, and lies at lighter densities ($\sigma_2 = 36.65$ kg m^{-3}, compared with 36.70 kg m^{-3} with CORE2 and 36.73 kg m^{-3} with DFS5.2). We note that Arctic and Nordic Seas waters do not appear to contribute significantly to the NADW that is exported southwards, despite the deep winter mixing seen north of 70°N in the CORE2 simulation, since no streamlines from the Arctic continue southward of 68°N: a known weakness of this model configuration is that much of the dense water that enters the subpolar gyre through the Denmark Strait and over the Iceland-Faeroes-Scotland Ridge is rapidly transformed by unphysically large numerical entrainment as it sinks south of the sills.

As discussed by Sidorenko et al. (2020, 2021), the overturning stream function represents the sum of processes, including surface buoyancy forcing, mixing, and also contributions from the nonlinear equation of state (cabbeling and thermobaricity). The use of the surface-forced stream function (lower panels) allows us to specifically identify the contribution of surface forcing to watermass transformations; the differences between the overturning and surface-forced stream functions may be understood as arising from a combination of mixing, cabbeling, thermobaricity, and truncation errors due to the use of monthly mean fields. Indeed, we see that the overall form of the overturning circulation is well explained by the surface forcing, with the exception of the continuing densification north of 65°N, contrasting with the overturning stream functions which do not display any southward transport for densities greater than $\sigma_2 = 37.1$ kg m^{-3}. We do not display the difference between the two stream functions here (as presented by Xu et al. (2018) and by Sidorenko et al. (2020, 2021)), since the truncation errors involved in calculating overturning and surface-forced stream functions offline would make evaluation of the difference between the two rather unreliable (we note that both the FESOM simulations and the HYCOM simulation described by Xu et al. calculate the stream functions online, whereas we use monthly means).

As reported by Marsh (2000) and others, there are two lobes in the surface-forced stream functions, corresponding to different locations of density transformation. In the simulations described here, Ψ_{surf} has two clear maxima in the CORE2-forced and DFS5.2-forced cases (Figures 3d and 3e), the upper lobe centered at $\sigma_2 \approx 36.40$ kg m^{-3}, typical of wintertime surface density in the eastern North Atlantic, associated with the formation of Subpolar Mode Water (SPMW), and the lower one at $\sigma_2 \approx 36.85$ kg m^{-3}, closer to winter densities in the Irminger Sea. In the JRA55-forced experiment, the lobes are not separated in density space, and the 19 Sv contour encloses both regions: comparison with Figures 2a–2c shows that mixing occurs to about 800-m depth south of the Faeroe Islands in CORE2 and DFS5.2, but not in JRA55, which is consistent with the weak upper lobe in Figure 3f. Further transformation occurs at densities above $\sigma_2 = 36.85$ kg m^{-3}, which we locate in the Labrador Sea, since this is the only location where such high surface densities are seen in the subpolar gyre, and this is associated with southward transport. So the overall picture is of a chain of densification, first described from observations by McCartney and Talley (1982), which is driven locally by wintertime surface buoyancy losses as water circulates cyclonically around the Subpolar Gyre: first in the north-east, forming SPMW, then in the Irminger Sea, and then finally in the Labrador Sea, resulting in the creation of the model's representation of North Atlantic Deep Water.

In the CORE2 and DFS5.2 experiments, the north-east Atlantic and Irminger cells are distinct, suggesting that there is a separate pathway for water of density between $\sigma_2 = 36.35$ and 36.5 kg m^{-3} that is created in the former region to be exported southward in these simulations, but the continuity between the Irminger and Labrador regions implies that a pathway exists for water created in the Irminger Sea to enter the Labrador Sea and then be transformed, possibly by a combination of surface processes and mixing, into the NADW with density higher than $\sigma_2 = 36.9$ kg m^{-3} which then propagates southwards as Upper North Atlantic Deep Water (UNADW). The

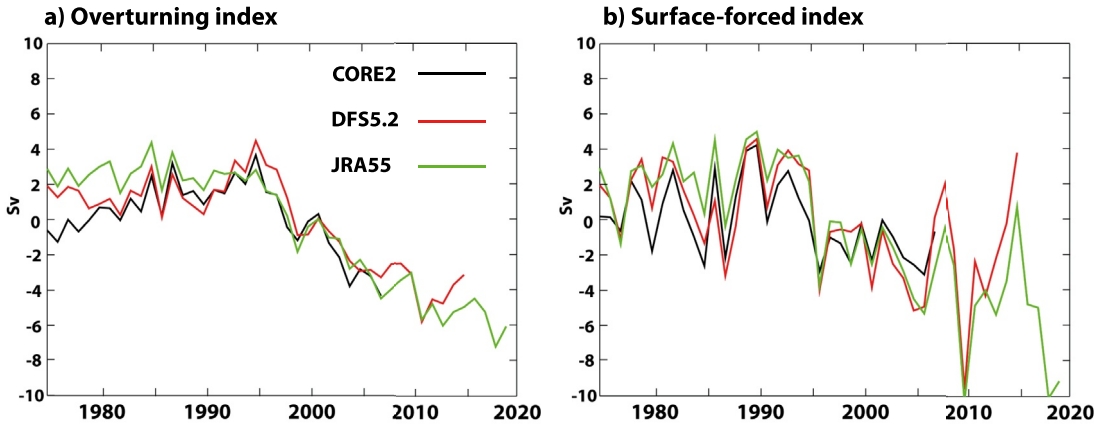

Figure 4. Time evolution of stream function indices for the three model integrations: (a) overturning strength and (b) surface-forced circulation. The indices have the mean from 1976 to 2005 subtracted.

UNADW is therefore formed in the Labrador Sea by a combination of local wintertime convection and mixing with water flowing in from the north-east Atlantic region and the Irminger Sea.

We now use the indices T_{OV} and T_{SF}, as defined in Section 3, to investigate the time dependence of the surface-forced circulation and to relate this to changes in the overturning strength. In Figures 4a and 4b, we show the time evolution of the two indices for each of the three model integrations, with the respective means from 1976 until the end of the integration subtracted. As observed by Grist et al. (2009) and Desbruyères et al. (2019), there is significantly more interannual variability in the surface-forced stream function T_{SF} than there is in the overturning circulation itself, as represented by T_{OV}; the interpretation is that changes in the latter result (at least partly) from accumulated surface buoyancy fluxes over a few years, which will smooth out such fluctuations. After 1975, all the indices can be seen to increase until the 1990s, after which they decline by about 5 Sv; comparison with Figure 1 confirms that this is consistent with the maximum overturning evaluated in depth space at both 26°N and 45°N. The three experiments again follow one another quite closely, with the JRA55-forced experiment indicating a continuing decline after 2015. The decadal-time scale evolution of both indices can be seen to be quite consistent between the three integrations, particularly the peak in the overturning strength in 1995 shown in Figure 1 and the subsequent decline. The latter decline is also clearly visible in the surface-forced indices (Figure 4a), but the maximum occurs earlier, with two peaks between 1989 and 1995. As already noted, there is considerable interannual variation in the surface-forced indices, with typical amplitude similar to that of the long-term changes, but the interannual variability is quite well correlated between the different forcing data sets.

4.3. Construction of a Surface-Forced Overturning Index

Josey et al. (2009) note a maximum correlation between the strength of the overturning and the maximum surface-forced stream function in a coupled model and the NCAR reanalysis, where the latter time series is lagged by between 6 and 15 years at 36°N, with the delay increasing toward higher latitudes, while the results of Desbruyères et al. (2019) suggest a shorter delay of between 3 and 6 years. Both these observations are consistent with a hypothesis that the overturning circulation is driven predominantly by the accumulated surface buoyancy loss from certain density classes over a handful of preceding years. To verify this for the model integrations described here, we define a synthetic surface-forced index T_{int} for a given year. To test the sensitivity to the time scale, we accumulate the surface-forced index T_{SF} in five different ways: as the mean of the surface-forced index over the preceding 5 and 10 years, respectively, with constant weights; and as means over 5, 10, and 15 years with the weights ramped up linearly from zero to a given year. Table 3 shows the correlation coefficients r between the respective unlagged overturning index T_{OV} and the synthetic surface-forced indices T_{int} for each of the experiments and the ensemble mean, the correlation evaluated over the period between 1976

Table 3
Correlations Between Surface-Forced Index and the Lagged Accumulated Indices for Each of the Experiments and for the Ensemble Mean

Forcing	CORE2	DFS5.2	JRA-55	Ensemble mean
Zero lag	0.537	0.660	0.858	0.786
Five-year box	0.766	0.912	0.953	0.935
Ten-year box	0.819	0.898	0.956	0.954
Five-year ramp	0.743	0.900	0.955	0.927
Ten-year ramp	0.859	0.940	0.970	0.968
Fifteen-year ramp	0.863	0.929	0.966	0.965

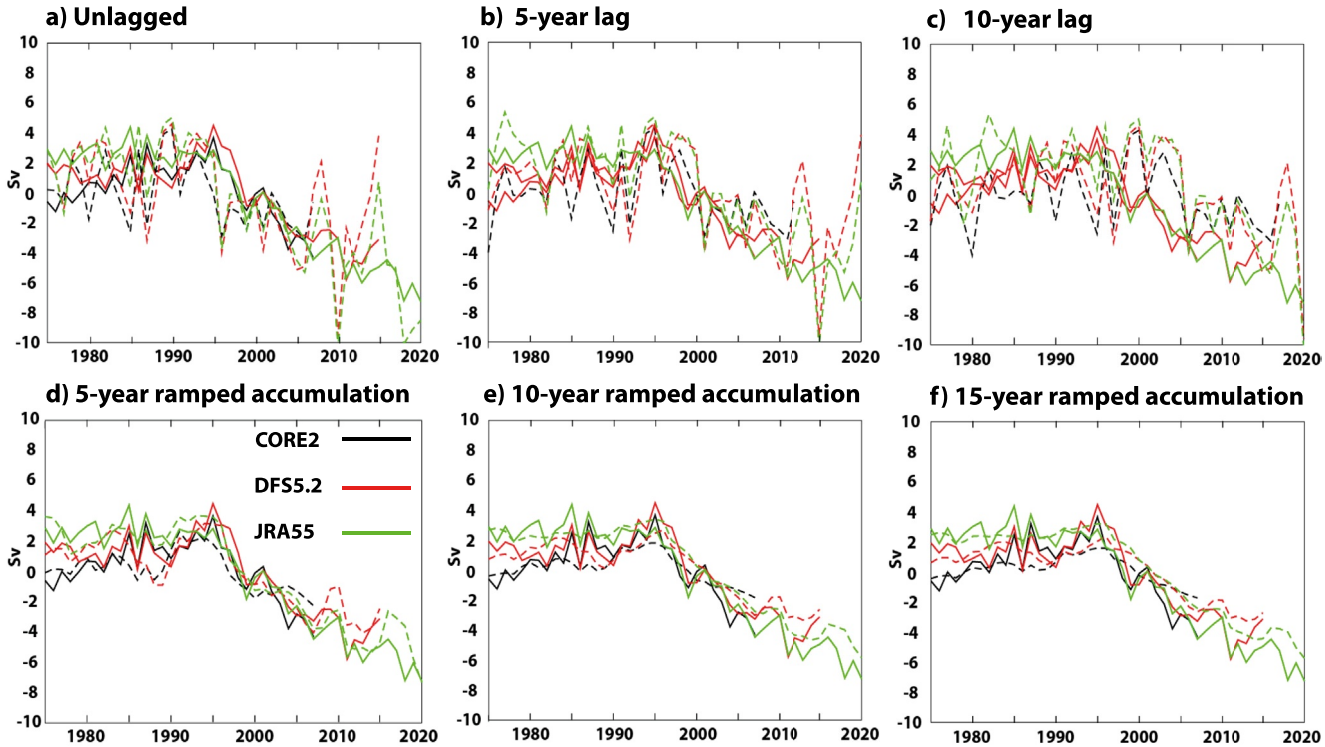

Figure 5. Overturning index T_{OV} (solid lines) with surface-forced index T_{SF} delayed by (a) 0 years; (b) 5; and (c) 10 years; and accumulated overturning indices (dashed lines) with surface-forced indices averaged over (d) the previous 5 years with ramped weights; (e) the previous 10 years with ramped weights; and (f) the previous 15 years with ramped weights.

and the end of the respective time series. The correlation coefficients are consistently highest for the 10-year ramp and the 15-year ramp, with lower coefficients obtained for shorter time scales for the accumulation. The correlation coefficients for the 10-year and 15-year ramped accumulations lie in the range from 0.86 to 0.96, so the fraction of the variance of the overturning index T_{OV} explained by the surface-forced index T_{surf} is the square of these coefficients, and is therefore between 0.74 and 0.92. Estimating the effective sample size N_{eff} for correlated time series, as defined by Bretherton et al. (1999) from autocorrelations of each of the time series (not shown), we find values of N_{eff} of between 7 and 10 for the three time series, for which the Pearson critical value is between 0.57 and 0.66, so the correlation coefficients for all of the accumulated indices in Table 3 may be judged robust.

In Figure 5, we show the overturning index for each of the integrations, overlain with the surface-forced index lagged by 0, 5, and 10 years (panels (a)–(c)), and the overturning index with the integral index T_{int} accumulated using a 5-year box with constant weights, a 10-year ramp, and a 15-year ramp (Figures 5d, 5e and 5f, respectively). As noted in the forementioned studies, the lagged surface-forced index follows the overturning index over decadal time scales, but it is noisy on interannual frequencies, with steps of up to 4 Sv between successive years; its usefulness as a predictor of overturning changes is therefore limited, regardless of the lag chosen. The integral index, however, tracks the overturning strength much more closely, especially using the 10-year ramp (Figure 5e), which not only echoes the decadal changes in overturning strength but also shows some agreement in the interannual variations. We conclude that the 10-year and 15-year ramped accumulations give qualitatively closer agreement between this surface-forced index and the overturning index, implying a characteristic time scale of between 5 and 7.5 years for the surface fluxes to drive changes in the overturning, consistent with the longer time scales of up to 10 years observed by Josey et al. (2009).

4.4. Geographical Distribution of Surface Buoyancy Loss

We now examine the connection between decadal changes in the overturning strength and the components of the buoyancy flux in the regions of dense water formation in the subpolar North Atlantic and the Nordic Seas, as defined in Table 2. In each region, we evaluate the wintertime (DJF) buoyancy loss in kg m^{-3} s^{-1} from monthly

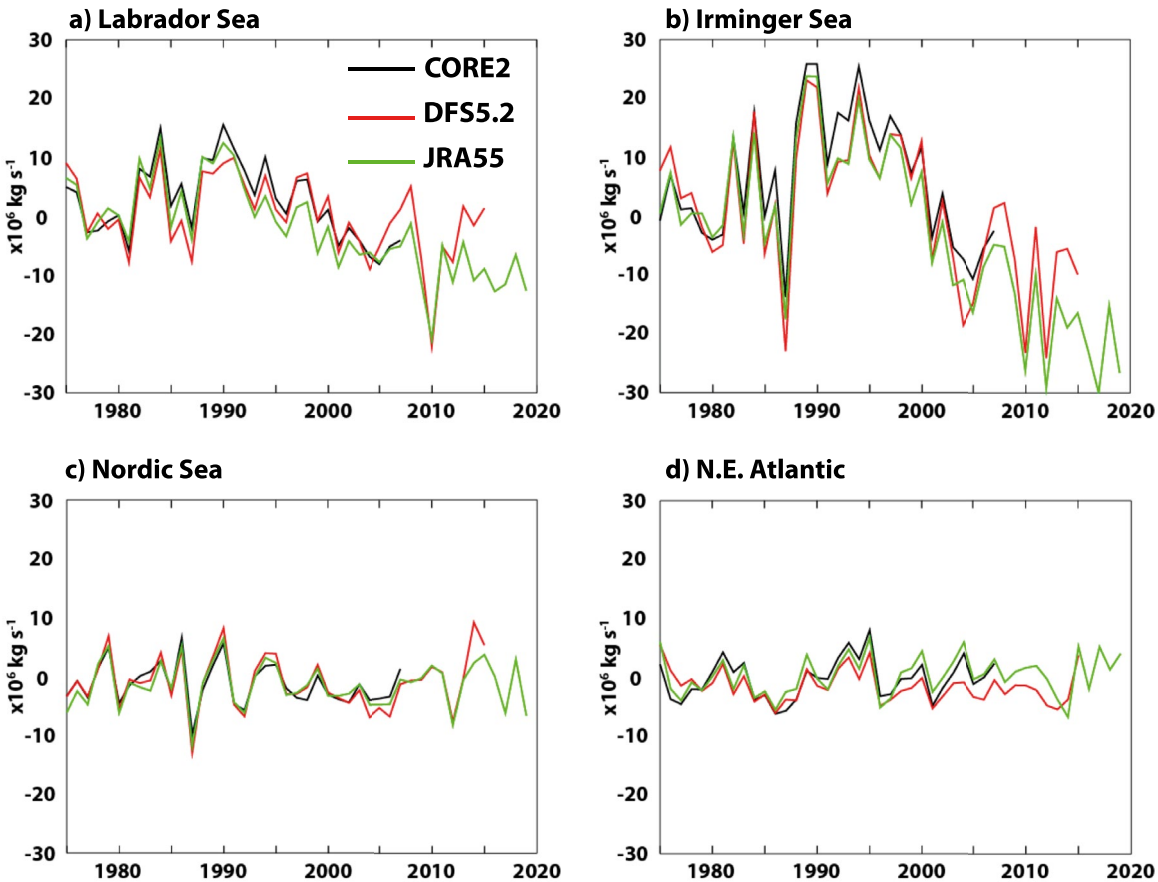

Figure 6. Wintertime (DJF) buoyancy loss anomalies ($\times 10^6$ kg s^{-1}) from monthly mean heat flux, integrated over (a) the Labrador Sea; (b) the Irminger Sea; (c) the north-east Atlantic; and (d) the Nordic Seas in each experiment, with respect to the mean from 1976 to the end of the respective integration.

mean heat and freshwater fluxes according to Equation 1 and integrate over the respective ocean surface area. We find that the variability of the buoyancy contributions from the freshwater flux is negligible, in comparison with that from the surface cooling: the standard deviations of the latter all lie below 0.3×10^6 kg s^{-1}, where those of the former are all above 3.0×10^6 kg s^{-1}, so we only show here the contribution from heat loss. We emphasize that we only address here the variability in each contribution: our conclusion that variations in freshwater fluxes do not contribute significantly to the decadal changes in overturning strength certainly does not imply that the time-averaged freshwater fluxes are not important to the overturning circulation. Figure 6 shows the anomalies of the contributions of the heat flux to area-integrated buoyancy loss anomalies over each of the four basins with respect to the 1976–2005 mean, all with the same vertical scale. It may be noted immediately that the evolution of the heat loss from the Irminger Sea (Figure 6b) is strikingly similar to that of the stream function indices, as well as to that of the AMOC at both 26°N and 45°N, with a clear increase to 1990, followed by an unambiguous decline from then until at least 2010. The heat loss from the Labrador Sea (Figure 4a) has a similar evolution, but the signal is less than half of that of the heat loss from the Irminger Basin. The buoyancy losses in the Nordic Seas and in the north-east Atlantic (Figures 4c and 4d) have little interdecadal variability, and so these regions contribute little to the long-term changes seen in the overturning circulation. Again, we only discuss the variability, rather than the time-average of these regional heat fluxes: Figure 3 confirms that there is indeed a strong mean buoyancy loss in the Nordic Seas, even if the variability in time is small.

4.5. Attribution of Winter Buoyancy Loss to Physical Processes

In Section 4.3, we showed that decadal-time scale variations in the AMOC are highly correlated with variations in the strength of the surface-forced stream function, when the latter is accumulated over a time scale of around 10 years, which strongly implies that the surface fluxes are the cause of the changes in the overturning strength.

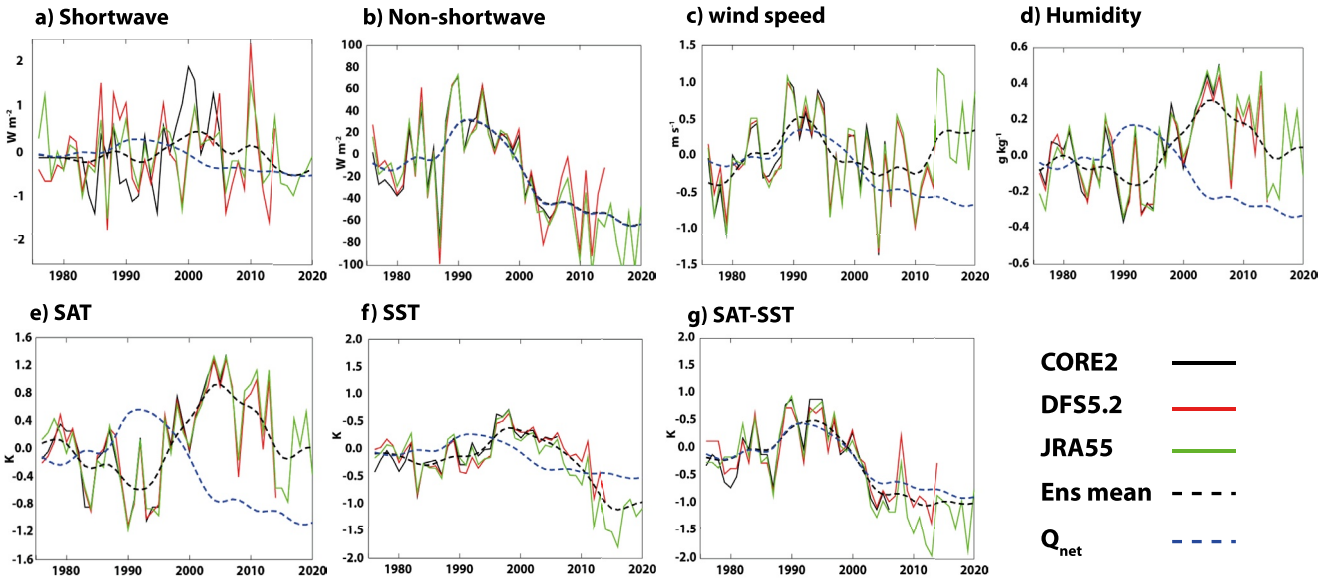

Figure 7. Wintertime (DJF) anomalies from the 1976 to 2005 means of surface fields averaged over the Irminger Sea from the experiments: (a) shortwave radiation; (b) total upward heat flux minus the shortwave component; (c) wind speed; (d) near-surface specific humidity; (e) near-surface air temperature; (f) sea surface temperature; and (g) sea surface temperature minus air temperature. The dashed black line on each panel is the ensemble mean over all the fields available in a given year, with a Gaussian windowed low-pass filter with half-width 5 years, for each quantity. The dashed blue lines show the upward winter surface heat flux anomaly, also low-pass filtered and normalized to have the same variance as the respective index, for comparison.

In Section 4.4, we demonstrated that the variability in area-integrated buoyancy losses is dominated by changes in the wintertime heat loss from the Irminger Sea, and to a lesser extent by heat loss in the Labrador Sea.

We now address the question of what the proximal causes are of the changes in heat loss in the Irminger and Labrador Seas. In this section, we shall present time series of the regional means of the relevant wintertime near-surface fields from each forcing data set, along with the respective ensemble mean, to indicate which surface processes are most likely to form the dominant contributions to the variability on the time scales we have discussed in previous sections.

Figure 7 shows anomalies of selected winter mean (DJF) surface fields, averaged over the Irminger Sea box, and defined with respect to the mean from 1976 to 2005. The bold dashed black lines are of the ensemble mean of each variable (in other words, the mean of the time series shown by the black, red, and green lines), with a Gaussian windowed low-pass filter of width 5 years applied, and the bold dashed blue lines show the anomaly of the winter upward heat flux out of the Irminger Sea, low-pass filtered as above, and normalized to have the same variance as the respective forcing field. We note in passing that the wind speed is defined at 10 m above sea level for all the data sets, while the air temperature and humidity are located at 10 m above sea level for CORE2 and JRA-55, and at 2 m for DFS5.2; we shall refer to the air temperature as "SAT" for brevity, even though the temperature is defined above the sea surface. All of the quantities except for the shortwave radiation are rather consistent between the three forcing data sets; the magnitude of the scatter in the latter quantity across forcing fields is low (of order 1 W m^{-2}) compared to the standard deviation of the net heat fluxes (over 30 W m^{-2}) and is dominated by interannual variability.

The heat loss anomaly (dashed blue lines) rises to a maximum in around 1992, then falls toward a minimum just before the end of the JRA-55 integration in 2019. The downwelling shortwave heat flux (Figure 7a) shows some of the same decadal variability as the net flux, and is in antiphase with the heat loss, but the magnitude of the variation, as remarked above, is only a few percent of that of the net flux. To definitively eliminate it as an important contribution to the decadal variability of the heat flux, we plot in Figure 7b the total heat flux minus the shortwave component: the anomaly of the residual (thick black dashed line) overlies the total heat flux anomaly (thick blue dashed line) almost perfectly, so we infer that the variability of the shortwave is indeed negligible in comparison to that of the sum of the latent, sensible, and longwave components. The air temperature (Figure 7c) and the humidity (Figure 7d) both vary in antiphase with the heat flux except in the period 2005–2015. With the

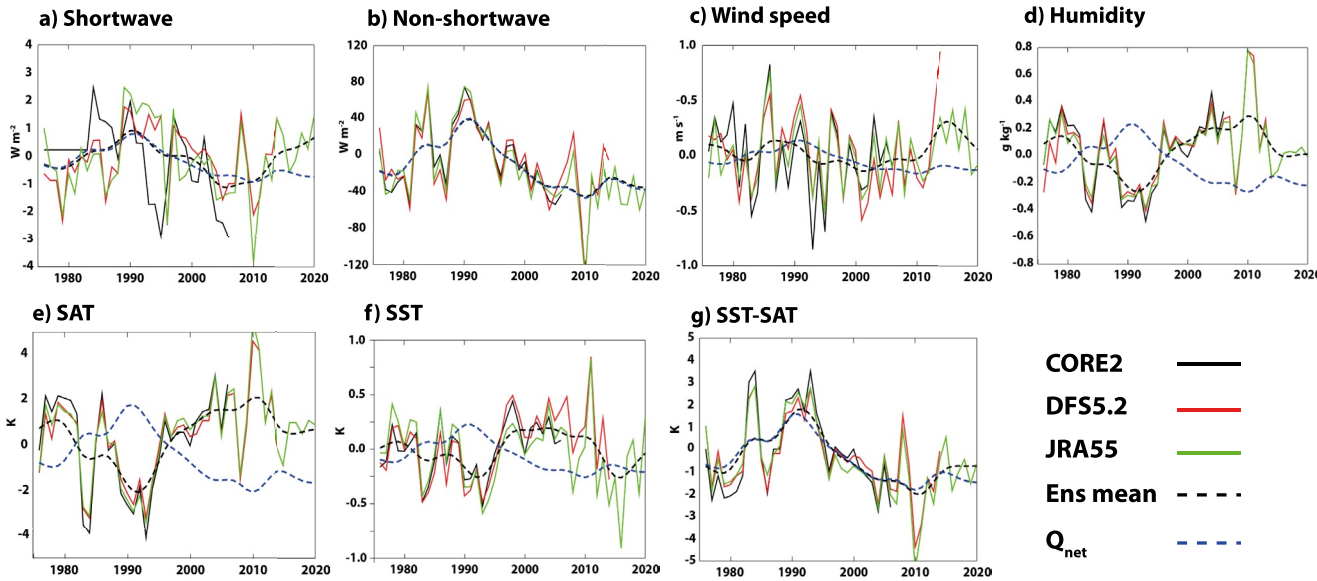

Figure 8. Wintertime (DJF) anomalies from the 1976 to 2005 means of surface fields averaged over the Labrador Sea from the experiments: (a) shortwave radiation; (b) total upward heat flux minus the shortwave component; (c) wind speed; (d) near-surface specific humidity; (e) near-surface air temperature; (f) sea surface temperature; and (g) sea surface temperature minus air temperature. The dashed black line on each panel is the ensemble mean over all the fields available in a given year, with a Gaussian windowed low-pass filter with half-width 5 years, for each quantity. The dashed blue lines show the upward winter surface heat flux anomaly, also low-pass filtered and normalized to have the same variance as the respective index, for comparison.

relatively short time series available, it is not straightforward to relate the SST anomaly (Figure 7e) causally to the heat flux: evaluation of lagged correlations gives maximum correlations of −0.9 with the SST leading the heat loss by 7 years, and +0.5 with SST lagging heat loss by 14 years. By contrast, the air-sea temperature difference (Figure 7f) follows the heat loss closely over the whole analysis period. The wind speed (Figure 7g), again has a similar evolution to the heat flux until 2000, after which it increases while the heat loss continues to reduce.

To summarize, variations of the net heat loss from the Irminger Sea on interannual-to-decadal time scales are closely correlated with variations of the air-sea temperature difference over the same region, throughout the analysis period from 1976 to 2020. Correlations between the heat flux and both the air temperature and wind speed are strong until 2005, after which stronger winds are partially compensated by warmer air temperatures. The sensible heat flux in the CORE bulk formulae used in the model (Large & Yeager, 2009) is proportional to the product of the air-sea temperature difference and the wind speed, while the latent heat flux is proportional to the product of the SST, the relative humidity (which itself closely follows the SST) and the wind speed, and the upwelling longwave flux is dependent on the SST alone. We conclude that the changes in heat flux are dominated by changes in the air temperature until about 2010, after which there is a strong feedback from the SST on the heat flux, and thence on the AMOC.

As noted in Section 4.4, the area-integrated buoyancy flux over the Labrador Sea evolves in a similar way to both the AMOC and the buoyancy loss from the Irminger Sea but with about half the magnitude of the latter. Figure 8 shows the same time series as Figure 7, but with means evaluated over the Labrador Sea. Again, the shortwave radiation plays a negligible part in the variability, and the closest time series to that of the net heat flux is that of the air-sea temperature difference, although the SST and SAT follow the heat flux much more closely than in the Irminger Sea. The SST here (Figure 8e) is much more strongly anticorrelated with the heat flux than in the Irminger Sea, which implies that the winter air temperature is more directly controlling the SST there, consistent with its closer proximity to the North American land mass.

4.6. Relationship of the AMOC to the NAO

We note that the decadal evolution of the AMOC in all three simulations, as shown in Figure 1, is similar to that of the observed North Atlantic Oscillation (NAO) index (e.g., Robson et al., 2018). The low-pass filtered index shown in Figure 1a of Robson et al. (2018), which is derived from the winter surface pressure difference between

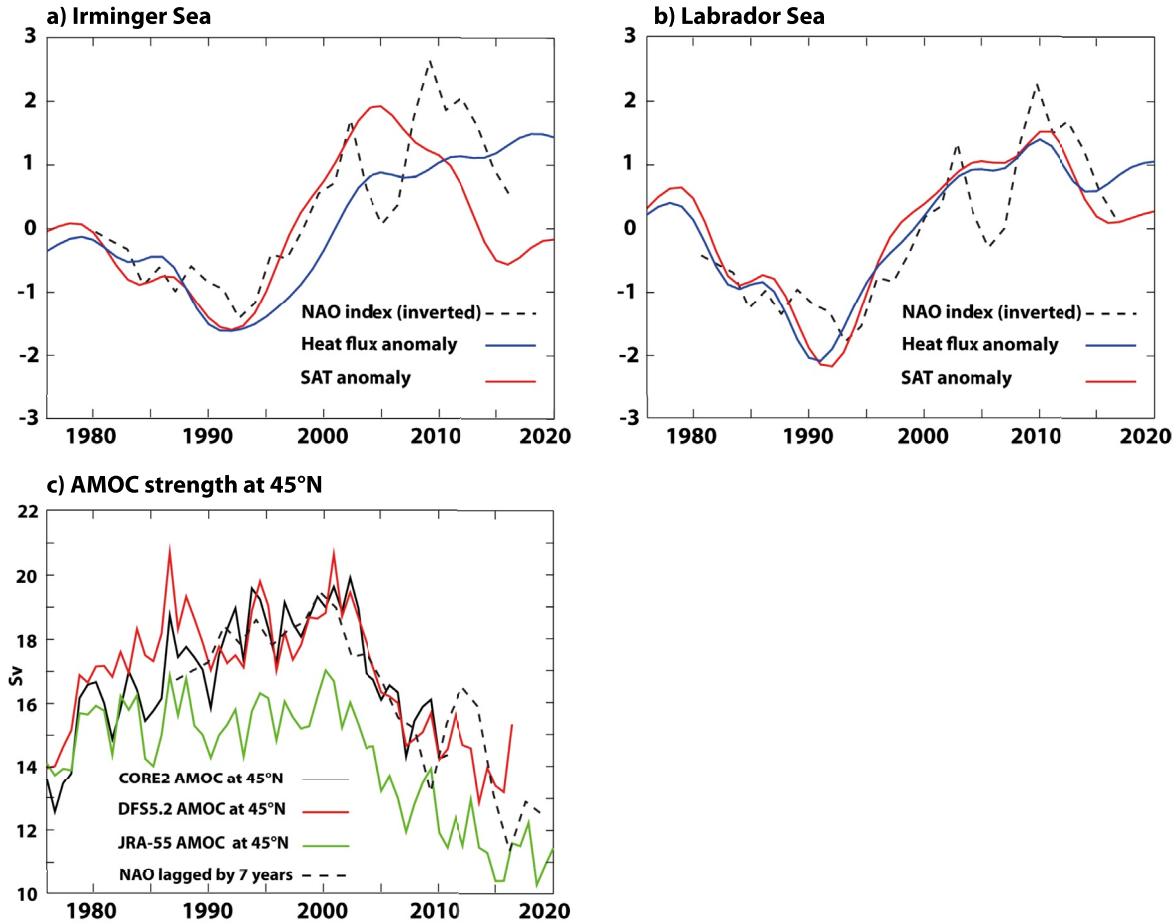

Figure 9. Normalized and low-pass filtered wintertime (DJF) anomalies of ensemble mean downward heat flux (blue line) and surface air temperature (red line) averaged (a) over the Irminger Sea and (b) over the Labrador Sea; along with the NAO index from Robson et al. (2018), inverted for consistency (dashed black line); and (c) the Atlantic meridional overturning circulation (AMOC) strength at 45°N in the three experiments, overlain with the NAO index delayed by 7 years (dashed black line).

Reykjavik and Gibraltar, increases to a positive maximum in the first half of the 1990s, is negative throughout the 2000s, then becomes positive in the mid-2010s. Parker et al. (2019) used the ERA-20C climatology (Poli et al., 2016) and the Met Office operational forecasting system GloSea5 (MacLachlan et al., 2015) to show that the path of the Jet Stream in the north-west Atlantic meanders on decadal time scales in a way that is strongly correlated with the winter NAO index: under typical positive NAO conditions the Jet Stream follows a more direct path across the North Atlantic, allowing cold Arctic air north of it to lie over the subpolar gyre, while under a negative NAO a blocking high pressure system tends to create a large northward meander onto Greenland to up to 80°N, bringing subtropical air over the subpolar gyre.

If the cold air outbreaks over the North Atlantic subpolar gyre typical under positive NAO conditions are associated with high heat loss over this region and if they, as we have shown, lead to a stronger AMOC over the following few years (and, conversely, if warmer air temperature in negative NAO phases leads to a reduced heat loss, followed by a weakening of the AMOC), there should be a strong correspondence between the NAO index and the SAT and heat flux indices presented in Figures 7 and 8. Figures 9a and 9b show the ensemble mean anomalies of the winter SAT and of the downward heat flux over the Irminger and Labrador Seas, respectively, normalized to unit variance and with the 5-year Gaussian low-pass filter applied as in Figures 7 and 8, along with the NAO index presented in Figure 1a of Robson et al. (2018), the latter index inverted for clarity. Over the Irminger Sea, the SAT varies with the inverted NAO quite closely, although it does not show the peak one would expect from the strong negative NAO in 2009, while the heat flux also broadly follows the NAO until the mid-2000s, but continues to increase despite the cooling air temperature. Over the Labrador Sea, there is a strong covariance between

all of the indices: the SAT and the heat flux reach a minimum in the early 1990s, aligned with the positive peak (here shown as a minimum) of the NAO, followed by an increase up to 2010 and a decline up to about 2015, with an upturn in the last 5 years. Finally, Figure 9c shows the AMOC at 45°N (taken from Figure 1b) overlain with the NAO index, the latter delayed by 7 years (the lag with maximum correlation): it is clear that the time evolution of the AMOC, with a peak at about 2000, followed by a decline up to about 2015, corresponds to a very similar evolution of the NAO. This time scale is consistent with the accumulation time of between 5 and 10 years identified in Section 4.3 between the surface forcing and the changes in overturning.

Robson et al. (2018) show (in their Figure 2c) that the winter Jet Stream latitude in the north-west Atlantic is correlated with the NAO index, lying predominantly north of its mean path until the mid-1990s, followed by a period until 2010 in which it lies south of the mean. They also show that the speed of the Jet Stream in the North Atlantic is strongly correlated with the NAO, with higher speeds corresponding to positive NAO phase. We interpret this as confirmation that the NAO is the dominant influence on the surface air temperature over the subpolar gyre, hence on the formation of Subpolar Mode Water and ultimately, through continuing buoyancy losses, on the forcing of the AMOC. As mentioned in the previous section, the SAT by itself does not explain the variability of the heat flux from 2000 to 2020, since the latter continues to fall after 2000, as do both the overturning and surface-forced indices shown in Figure 5e, while the SAT continues to cool (reflected in the upward trend in the red line in Figure 9). We therefore conclude that the changes in air temperature over the Irminger Sea associated with the NAO explain well the variation in the heat flux, and therefore the overturning, until 2000, after which the changes in heat flux are more faithfully explained by advective SST changes in the North Atlantic Current.

5. Summary and Discussion

Three integrations of 1/4° global NEMO, forced with CORE2, DFS5.2, and JRA55 data sets, have been completed from 1958 to as close to the present day as the forcing data permit; in particular, the simulation forced with JRA-55 extends to the end of 2020. We have identified decadal variation of AMOC strength from 1976 that increases up to 1990, then declines to the present, consistent with observed estimates. The three runs with different forcing data sets have consistent variability on interannual-to-decadal time scales, despite an overturning circulation with the JRA-55 forcing that is about 3 Sv weaker than with the other two forcing data sets.

To relate decadal-time scale variation in watermass formation to surface processes, we have calculated the overturning and surface-forced stream functions in potential density space, and have defined a pair of indices representing the maximum value of the respective annually averaged stream function in the region in density and latitude space of strongest density transformation. We find that an annual index, which we have defined as the surface-forced index averaged with weights falling linearly to zero over the preceding 10 years, matches the overturning index more closely than any simply lagged index, at the same time as smoothing out the considerable interannual variability. This indicates that the decadal variability of the overturning strength is primarily driven by buoyancy losses accumulated over this time scale. The density transformations revealed by the overturning stream function give a picture of successive densification around the subpolar gyre that is consistent for all three integrations: subpolar mode water formed in the north-east Atlantic with σ_2 between 36.3 and 36.6 kg s^{-1} is advected into the Irminger Sea, where surface buoyancy loss increases the density to between 36.5 and 36.9, and this is subsequently transformed in the Labrador Sea to Upper North Atlantic Deep Water with densities between 36.9 and 37.0 kg s^{-1} and then exported southwards, as described by McCartney and Talley (1982). In the simulations there is negligible dense Arctic water present in the NADW, despite substantial cooling and convection in the Nordic Seas south of Svalbard, which is likely to be a result of poor representation of Arctic waters upstream of Denmark Strait and of the Iceland-Faeroes-Scotland ridge system, along with excessive numerical mixing in the overflows. It is uncertain how this model limitation affects the results presented here; for the most part, the overflow waters contribute to denser watermasses than those discussed here, although in the real ocean there is significant entrainment of the overflow water with the lighter waters overlying it. The surface heat loss over the Nordic Seas shows little variability (Figure 6c), so the surface fluxes over the Labrador and Irminger Seas would still be expected to dominate the AMOC variability.

Evaluation of winter (DJF) means of area-integrated buoyancy fluxes in four regions of wintertime convection (the Labrador Sea, the Irminger Sea, the north-east Atlantic, and the Nordic Seas) shows that the variability seen in the overturning strength is mainly due to variation of the heat loss over the Irminger Sea, with the variability

of the buoyancy loss from cooling over the Labrador Sea having half the magnitude, while neither cooling of the north-east Atlantic and Nordic Seas, nor freshwater fluxes in any of the regions, has any significant variability, even though the mean values in these regions may be substantial. We therefore conclude that the variability in the AMOC is largely driven by variability in winter heat loss, mainly over the Irminger Sea, but to a lesser extent over the Labrador Sea. This variability is imprinted on the AMOC as a modulation of the volume of dense water formed in the latter two basins as it moves in a cyclonic sense around the subpolar gyre; the lag of between 5 and 10 years between the surface flux variations and the AMOC is likely to result from a combination of the accumulation of modifications to the ocean density over several winters, and delays due to the advection of density anomalies along interior pathways. The time scale for the first process is consistent with the observations of Desbruyères et al. (2020), who noted that surface temperature anomalies in the EN4 data set took between 5 and 10 years to penetrate to 1,000 m as they propagated around the subpolar gyre, while Yashayaev et al. (2007) identified transit times of up to 5 years for anomalies in dense water at 1100-m depth to recirculate from the Labrador Sea to the Irminger Sea.

The time evolution of each of the surface forcing fields was compared to that of the net heat flux over the Irminger Sea, and a strong correlation was found with the air-sea temperature difference, and to a lesser degree with the surface humidity and the wind speed, while the variability of the solar shortwave radiation was found to be very low by comparison. This implies that on decadal time scales the air temperature was the main driver of changes in buoyancy losses over the Irminger Sea, and subsequent changes in the AMOC until around the year 2000, when the AMOC changes caused subpolar SST changes, triggering a positive feedback that maintains the AMOC decline. The sensitivity to air temperature, along with the fact that the AMOC anomaly follows that of the North Atlantic Oscillation index, suggests that the two most likely mechanisms for AMOC variability are meandering of the Jet Stream that brings alternately warm and cold air over the subpolar Irminger Sea; and variation of the speed of the Jet Stream that is associated with changes in advection of cold continental air masses over the subpolar North Atlantic, both processes strongly correlated with the NAO.

The use of the density transformation framework, and more specifically the surface-forced stream function, provides strong insights into the relationship between changes in surface buoyancy fluxes and changes in watermass properties that are not directly provided by analysis of the overturning in depth coordinates, nor by calculation of winter mixed-layer depths alone. It sidesteps questions regarding the representation of convection in numerical models (they generally use an enhanced diffusivity to mix to a prescribed depth, which is a distinct physical process from convection), and also disregards the issue of preconditioning for convection by salty anomalies in the upper ocean (e.g., Menary et al., 2012; Ortega et al., 2021). As we have demonstrated, the surface-forced stream function can in addition be used to derive a scalar index that has predictive skill for the overturning strength. Nevertheless, the density transformation analysis we have presented has its limitations. The stream functions are constructed as zonal integrals, so lose information on the longitudinal location of the buoyancy losses, and also depend on a sufficiently long integration to remove enough noise from the signal for it to be interesting, at the same time as needing possibly impractically short averaging times (almost certainly shorter than the monthly means used here) to faithfully capture extreme buoyancy loss events such as those caused by the Greenland tip jets described by Josey et al. (2019). Extension of this framework to derive transformation rates as a two-dimensional field on given density surfaces, as derived from observational data by Desbruyères et al. (2019) and from numerical models by Xu et al. (2018) and Sidorenko et al. (2021) can provide much more detailed information on the processes of density transformation, but we have not evaluated these fluxes here.

There have been recent suggestions that the AMOC is currently in a recovery phase after the decline reported by Smeed et al. (2018) and others. The overturning and surface-forced indices derived by Desbruyères et al. (2019) from observational data sets show a decline of about 3 Sv from 1993 to 2010, followed by a sharp increase of about 4 Sv between 2010 and 2018. Moat et al. (2020) used data from the RAPID array at 26°N to estimate a recovery of a similar magnitude over the same period. This is not seen robustly in our simulations: the AMOC strength at both 26°N and 45°N in the JRA-55 forced experiment (the green lines in Figure 1) shows a continuing decline of about 2 Sv from 2010 to 2020, possibly leveling out in the final years, while that with DFS5.2 suggests a possible increase after 2020. The overturning indices we have derived from the surface buoyancy fluxes (Figure 5e) are equivocal: while those for JRA-55 are consistent with the continuing weakening in the AMOC in that experiment, those for the DFS5.2-forced simulation suggest an upturn after 2010, although the latter data set ends in 2015, so robust conclusions may not be reached. Applying the analysis presented here to integrations forced

by a different forcing data set, such as ERA-5 (Hersbach et al., 2020), is likely to strengthen any predictions, and work by the authors to investigate this is underway using an ensemble based on a more recent 1/4° NEMO configuration. Nevertheless, we have clearly demonstrated the potential of this technique as a predictive tool for the AMOC strength, and the availability of surface field data sets that are continuously updated to a few months behind the present.

Appendix A: Code Documentation

The ocean model code is available from the NEMO website (www.nemo-ocean.eu) under the CeCILL free software license (http://www.cecill.info/). On registering, individuals can access the Fortran code using the open-source subversion software (http://subversion.apache.org/). The base code used for the integrations presented in this paper is in revision 7750 of the following branch: http://forge.ipsl.jussieu.fr/nemo/svn/NEMO/branches/UKMO/dev_r5518_GO6_package

This consists of the NEMO v3.6 release with the addition of GO6-specific changes. The sea-ice model code is freely available from the Met Office Science Repository (https://code.metoffice.gov.uk/trac/cice) under the CICE copyright agreement (http://oceans11.lanl.gov/trac/CICE/wiki/CopyRight) and the Fortran code is available using subversion. The code used for the integrations presented in this paper consisted of a number of branches of the CICE code. These branches have subsequently been merged into a single package branch (vn5.1.2_GSI8.0_package_branch) at revision 235.

The following preprocessing keys were applied in building GO6-GSI8.1: key_trabbl; key_si3; key_zdftke; key_zdfddm; key_mpp_mpi; key_mpp_rep; key_nosignedzero; key_iomput

Data Availability Statement

The output from the integrations described here is archived by the British Oceanographic Data Centre (BODC) at the Centre for Environmental Data Analysis (CEDA). It is available as follows: Megann et al. (2021a, 2021b, 2021c).

Acknowledgments

The work was supported by funding from the Natural Environment Research Council (NERC) under the Atlantic Climate System Integrated Study (ACSIS) project (NE/N018044/1), with additional funding from European Union's Horizon 2020 research and innovation programme COMFORT (Grant Agreement No. 820989) and additional support by the NERC WISHBONE project (reference NE/T013540/1). The model integrations were completed on the Archer supercomputing system and on the NEXCS platform at the UK Met Office, both facilities funded by NERC and the Engineering and Physical Science Research Council (EPSRC). Analysis was carried out on the JASMIN platform, funded by NERC. The authors are grateful for invaluable assistance from Computational Modeling Services at the National Centre for Atmospheric Science. The authors are grateful for the comments and suggestions from the three anonymous reviewers, which have substantially improved the paper. We would also like to thank Ed Blockley, Jeremy Grist, Joel Hirschi, Ben Moat, Jon Robson, and Dave Storkey for advice and assistance, and Richenda Houseago-Stokes and Helen Snaith for archiving the model output to BODC.

References

Arias, P. A., Bellouin, N., Coppola, E., Jones, R.G., Krinner, G., Marotzke, J., et al. (2021). Technical Summary. In *Climate change 2021: The physical science basis. Contribution of working Group I to the Sixth Assessment report of the intergovernmental panel on climate change*. Cambridge University Press.

Bigg, G. R., Wadley, M. R., Stevens, D. P., & Johnson, J. A. (1997). Modelling dynamics and thermodynamics of icebergs. *Cold Regions Science and Technology*, *26*, 113–135. https://doi.org/10.1016/s0165-232x(97)00012-8

Bitz, C. M., Holland, M. M., Weaver, A. J., & Eby, M. (2001). Simulating the ice-thickness distribution in a coupled climate model. *Journal of Geophysical Research*, *106*, 2441–2463. https://doi.org/10.1029/1999JC000113

Bitz, C. M., & Lipscomb, W. H. (1999). An energy-conserving thermodynamic model of sea ice. *Journal of Geophysical Research*, *104*, 15669–15677. https://doi.org/10.1029/1999JC900100

Bleck, R., & Sun, S. (2004). Diagnostics of the oceanic thermohaline circulation in a coupled climate model. *Global and Planetary Change*, *40*, 233–248. https://doi.org/10.1016/j.gloplacha.2003.04.002

Bretherton, C. S., Widmann, M., Dymnikov, V. P., Wallace, J. M., & Bladé, I. (1999). The effective number of spatial degrees of freedom of a time-varying field. *Journal of Climate*, *12*, 1990–2009. https://doi.org/10.1175/1520-0442(1999)012<1990:tenosd>2.0.co;2

Chafik, L., & Rossby, T. (2019). Volume, heat, and freshwater divergences in the subpolar North Atlantic suggest the Nordic Seas as key to the state of the meridional overturning circulation. *Geophysical Research Letters*, *46*, 4799–4808. https://doi.org/10.1029/2019GL082110

Chanut, J., Barnier, B., Large, W., Debreu, L., Penduff, T., Molines, J.-M., & Mathiot, P. (2008). Mesoscale eddies in the Labrador Sea and their contribution to convection and restratification. *Journal of Physical Oceanography*, *38*, 1617–1643. https://doi.org/10.1175/2008jpo3485.1

Cheng, W., Chiang, J. C. H., & Zhang, D. (2013). Atlantic meridional overturning circulation (AMOC) in CMIP5 models: RCP and historical simulations. *Journal of Climate*, *26*, 7187–7197. https://doi.org/10.1175/JCLI-D-12-00496.1

Curry, R. G., McCartney, M. S., & Joyce, T. M. (1998). Oceanic transport of subpolar climate signals to mid-depth subtropical waters. *Nature*, *391*, 575–577. https://doi.org/10.1038/35356

Danabasoglu, G., Yeager, S. G., Kwon, Y.-O., Tribbia, J. J., Phillips, A. S., & Hurrell, J. W. (2012). Variability of the Atlantic meridional overturning circulation in CCSM4. *Journal of Climate*, *25*(15), 5153–5172. https://doi.org/10.1175/JCLI-D-11-00463.1

Delworth, T., Zeng, F., Vecchi, G., Yang, X., Zhang, L., & Zhang, R. (2016). The North Atlantic Oscillation as a driver of rapid climate change in the Northern Hemisphere. *Nature Geoscience*, *9*, 509–512. https://doi.org/10.1038/ngeo2738

Desbruyères, D. G., Maze, G., Daniault, M., & Daniault, N. (2019). Surface predictor of overturning circulation and heat content change in the subpolar North Atlantic. *Ocean Science*, *15*, 809–817. https://doi.org/10.5194/os-15-809-2019

Desbruyères, D. G., Sinha, B., McDonagh, E. L., Josey, S. A., Holliday, N. P., Smeed, D. A., et al. (2020). Importance of boundary processes for heat uptake in the Subpolar North Atlantic. *Journal of Geophysical Research: Oceans*, *125*, e2020JC016366. https://doi.org/10.1029/2020JC016366

Dong, B., & Sutton, R. T. (2005). Mechanism of interdecadal thermohaline circulation variability in a coupled ocean-atmosphere GCM. *Journal of Climate*, *18*(8), 1117–1135. https://doi.org/10.1175/JCLI3328.1

Dussin, R., Barnier, B., & Brodeau, L. (2016). *The making of Drakkar forcing set DFS5. DRAKKAR/MyOcean Report 01-04-16*. LGGE.
Eden, C., & Willebrand, J. (2001). Mechanism of interannual to decadal variability of the North Atlantic circulation. *Journal of Climate*, *14*, 2266–2280. https://doi.org/10.1175/1520-0442(2001)014<2266:moitdv>2.0.co;2
Gaspar, P., Grégoris, Y., & Lefevre, J.-M. (1990). A simple eddy kinetic energy model for simulations of the oceanic vertical mixing: Tests at Station Papa and long-term upper ocean study site. *Journal of Geophysical Research*, *95*, 16179–16193. https://doi.org/10.1029/JC095iC09p16179
Grist, J. P., Josey, S. A., & Marsh, R. (2012). Surface estimates of the Atlantic overturning in density space in an eddy-permitting ocean model. *Journal of Geophysical Research*, *117*, C06012. https://doi.org/10.1029/2011JC007752
Grist, J. P., Josey, S. A., Marsh, R., Kwon, Y.-O., Bingham, R. J., Blaker, A. T., & Blaker, A. T. (2014). The surface-forced overturning of the North Atlantic: Estimates from modern era atmospheric reanalysis datasets. *Journal of Climate*, *27*, 3596–3618. https://doi.org/10.1175/JCLI-D-13-00070.1
Grist, J. P., Marsh, R. A., & Josey, S. A. (2009). On the relationship between the north Atlantic meridional overturning circulation and the surface-forced overturning streamfunction. *Journal of Climate*, *22*, 4989–5002. https://doi.org/10.1175/2009jcli2574.1
Hersbach, H., Bell, B., Berrisford, P., Hirahara, S., Horányi, A., Muñoz-Sabater, J., et al. (2020). The ERA5 global reanalysis. *Quarterly Journal of the Royal Meteorological Society*, *146*, 1999–2049. https://doi.org/10.1002/qj.3803
Hunke, E. C., & Dukowicz, J. K. (1997). An elastic-viscous-plastic model for sea ice dynamics. *Journal of Physical Oceanography*, *27*, 1849–1867.
Hunke, E. C., & Lipscomb, W. H. (2010). *Cice: The Los Alamos Sea ice model, documentation and software user's manual, version 4.1 (Tech. Rep.)*. Los Alamos National Laboratory. Retrieved from http://oceans11.lanl.gov/trac/CICE
Ingleby, B., & Huddleston, M. (2007). Quality control of ocean temperature and salinity profiles—Historical and real-time data. *Journal of Marine Systems*, *65*, 158–175. https://doi.org/10.1016/j.jmarsys.2005.11.019
Jackson, L., Dubois, C., Forget, G., Haines, G., Harrison, M., Iovino, D., et al. (2019). The mean state and variability of the North Atlantic circulation: A perspective from ocean reanalyses. *Journal of Geophysical Research: Oceans*, *124*, 9141–9170. https://doi.org/10.1029/2019JC015210
Josey, S. A., de Jong, M. F., Oltmanns, M., Moore, G. K., & Weller, R. A. (2019). Extreme variability in Irminger Sea winter heat loss revealed by ocean observatories initiative mooring and the ERA5 reanalysis. *Geophysical Research Letters*, *46*, 293–302. https://doi.org/10.1029/2018GL080956
Josey, S. A., Grist, J. P., & Marsh, R. (2009). Estimates of meridional overturning circulation variability in the North Atlantic from surface density flux fields. *Journal of Geophysical Research*, *114*, C09022. https://doi.org/10.1029/2008JC005230
Katsman, C. A., Drijfhout, S. S., Dijkstra, H. A., & Spall, M. A. (2018). Sinking of dense North Atlantic waters in a global ocean model: Location and controls. *Journal of Geophysical Research: Oceans*, *123*, 3563–3576. https://doi.org/10.1029/2017JC013329
Kieke, D., & Yashayaev, I. (2015). Studies of Labrador Sea Water formation and variability in the subpolar North Atlantic in the light of international partnership and collaboration. *Progress in Oceanography*, *132*, 220–232. https://doi.org/10.1016/j.pocean.2014.12.010
Kostov, Y., Johnson, H. L., & Marshall, D. P. (2019). AMOC sensitivity to surface buoyancy fluxes: The role of air-sea feedback mechanisms. *Climate Dynamics*, *53*, 4521–4537. https://doi.org/10.1007/s00382-019-04802-4
Kuhlbrodt, T., Griesel, A., Montoya, M., Levermann, A., Hofmann, M., & Rahmstorf, S. (2007). On the driving processes of the Atlantic meridional overturning circulation. *Reviews of Geophysics*. *45*, RG2001. https://doi.org/10.1029/2004RG0001662007
Large, W. G., & Yeager, S. G. (2009). The global climatology of an interannually varying air-sea flux data set. *Climate Dynamics*, *33*, 341–364. https://doi.org/10.1007/s00382-008-0441-3
Lee, M.-M., Coward, A. C., & Nurser, A. G. (2002). Spurious diapycnal mixing of deep waters in an eddy-permitting global ocean model. *Journal of Physical Oceanography*, *32*, 1522–1535. https://doi.org/10.1175/1520-0485(2002)032<1522:sdmotd>2.0.co;2
Liu, W., Fedorov, A. V., Xie, S.-P., & Hu, S. (2020). Climate impacts of a weakened Atlantic Meridional Overturning Circulation in a warming climate. *Science Advances*, *6*, eaaz4876. https://doi.org/10.1126/sciadv.aaz4876
Lozier, M. S., Li, F., Bacon, S., Bahr, F., Bower, A. S., Cunningham, S. A., et al. (2019). A sea change in our view of overturning in the subpolar North Atlantic. *Science*, *363*, 516–521. https://doi.org/10.1126/science.aau6592
MacLachlan, C., Arribas, A., Peterson, K. A., Maidens, A., Fereday, D., Scaife, A. A., et al. (2015). Global Seasonal forecast system version5 (GloSea5): A high resolution seasonal forecast system. *Quarterly Journal of the Royal Meteorological Society*, *141*, 1072–1084. https://doi.org/10.1002/qj.2396
Madec, G. & the NEMO Team. (2017). Note du Pôle de modélisation. In: *NEMO ocean engine: Version 3.6 stable (No 27 ISSN No 1288–1619)*. Institut Pierre-Simon Laplace (IPSL). https://doi.org/10.5281/zenodo.3248739
Marsh, R. (2000). Recent variability of the North Atlantic thermohaline circulation inferred from surface heat and freshwater fluxes. *Journal of Climate*, *13*, 3239–3260. https://doi.org/10.1175/1520-0442(2000)013<3239:rvotna>2.0.co;2
Marsh, R., Ivchenko, V. O., Skliris, N., Alderson, S., Bigg, G. R., Madec, G., et al. (2015). NEMO-ICB (v1.0): Interactive icebergs in the NEMO ocean model globally configured at eddy-permitting resolution. *Geoscientific Model Development*, *8*, 1547–1562. https://doi.org/10.5194/gmd-8-1547-2015
Martin, T., & Adcroft, A. (2010). Parameterizing the fresh-water flux from land ice to ocean with interactive icebergs in a coupled climate model. *Ocean Modelling*, *34*, 111–124. https://doi.org/10.1016/j.ocemod.2010.05.001
Mauritzen, C. (1996). Production of dense overflow waters feeding the North Atlantic across the Greenland-Scotland Ridge. Part 1: Evidence for a revised circulation scheme. *Deep-Sea Research Part I Oceanographic Research Papers*, *43*, 769–806. https://doi.org/10.1016/0967-0637(96)00037-4
McCartney, M. S., & Talley, L. D. (1982). The subpolar mode water of the North Atlantic Ocean. *Journal of Physical Oceanography*, *12*, 1169–1188. https://doi.org/10.1175/1520-0485(1982)012<1169:tsmwot>2.0.co;2
Megann, A. (2018). Estimating the numerical diapycnal mixing in an eddy-permitting ocean model. *Ocean Modelling*, *121*, 19–33. https://doi.org/10.1016/j.ocemod.2017.11.001
Megann, A., Sinha, B., & Blaker, A. (2021a). *Monthly ocean and sea-ice output from 1/4° NEMO GO6 integration forced by CORE2 data*. NERC EDS British Oceanographic Data Centre.
Megann, A., Sinha, B., & Blaker, A. (2021b). *Monthly ocean and sea-ice output from 1/4° NEMO (GO6 integration forced by DFS5.2 data*. NERC EDS British Oceanographic Data Centre.
Megann, A., Sinha, B., & Blaker, A. (2021c). *Monthly ocean and sea-ice output from 1/4° NEMO GO6 integration forced by JRA55 data*. NERC EDS British Oceanographic Data Centre.
Megann, A., & Storkey, D. (2021). Exploring viscosity space in an eddy-permitting global ocean model: Is viscosity a useful control for numerical mixing? *Journal of Advances in Modeling Earth Systems*, *13*, e2020MS002263. https://doi.org/10.1029/2020MS002263
Menary, M. B., Jackson, L. C., & Lozier, M. S. (2020). Reconciling the relationship between the AMOC and Labrador Sea in OSNAP observations and climate models. *Geophysical Research Letters*, *47*, e2020GL089793. https://doi.org/10.1029/2020GL089793

Menary, M. B., Park, W., Lohmann, K., Vellinga, M., Palmer, M. D., Latif, M., & Jungclaus, J. H. (2012). A multimodel comparison of centennial Atlantic meridional overturning circulation variability. *Climate Dynamics*, *38*(11–12), 1–12. https://doi.org/10.1007/s00382-011-1172-4

Menary, M. B., Robson, J., Allan, R., Booth, B. B. B., Cassou, C., Gastineau, G., et al. (2020). Aerosol-forced AMOC changes in CMIP6 historical simulations. *Geophysical Research Letters*, *47*, e2020GL088166.

Moat, B. I., Smeed, D. A., Frajka-Williams, E., Desbruyères, D. G., Beaulieu, C., Johns, W. E., et al. (2020). Pending recovery in the strength of the meridional overturning circulation at 26°N. *Ocean Science*, *16*(4), 863–874. https://doi.org/10.5194/os-16-863-2020

Ortega, P., Robson, J., Sutton, R. T., & Andrews, M. B. (2017). Mechanisms of decadal variability in the Labrador Sea and the wider North Atlantic in a high-resolution climate model. *Climate Dynamics*, *49*(7), 2625–2647. https://doi.org/10.1007/s00382-016-3467-y

Ortega, P., Robson, J. I., Menary, M., Sutton, R. T., Blaker, A., Germe, A., et al. (2021). Labrador Sea subsurface density as a precursor of multidecadal variability in the North Atlantic: A multi-model study. *Earth System Dynamics*, *12*(2), 419–438. https://doi.org/10.5194/esd-12-419-2021

Otterå, O., Bentsen, M., Drange, H., & Suo, L. (2010). External forcing as a metronome for Atlantic multidecadal variability. *Nature Geoscience*, *3*, 688–694. https://doi.org/10.1038/ngeo955

Parker, T., Woollings, T., Weisheimer, T., O'Reilly, C. H., Baker, L., Shaffrey, L., & Shaffrey, L. (2019). Seasonal predictability of the winter North Atlantic Oscillation from a jet stream perspective. *Geophysical Research Letters*, *46*, 10159–10167. https://doi.org/10.1029/2019GL084402

Peings, Y., & Magnusdottir, G. (2014). Forcing of the wintertime atmospheric circulation by the multidecadal fluctuations of the North Atlantic Ocean. *Environmental Research Letters*, *9*(3), 034018. https://doi.org/10.1088/1748-9326/9/3/034018

Petit, T., Lozier, M. S., Josey, S. A., & Cunningham, S. A. (2020). Atlantic deep water formation occurs primarily in the Iceland Basin and Irminger Sea by local buoyancy forcing. *Geophysical Research Letters*, *47*, e2020GL091028. https://doi.org/10.1029/2020GL091028

Pickart, R. S., Straneo, F., & Moore, G. W. K. (2003). Is Labrador Sea water formed in the Irminger Basin? *Deep-Sea Research I*, *50*, 23–52. https://doi.org/10.1016/s0967-0637(02)00134-6

Poli, P. H., Hersbach, H., Dee, D. P., Berrisford, P., Simmons, A. J., Vitart, F., et al. (2016). ERA-20C: An atmospheric reanalysis of the twentieth century. *Journal of Climate*, *29*(11), 4083–4097. https://doi.org/10.1175/jcli-d-15-0556.1

Ridley, J. K., Blockley, E. W., Keen, A. B., Rae, J. G. L., West, A. E., & Schroeder, D. (2018). The sea ice model component of HadGEM3-GC3.1. *Geoscientific Model Development*, *11*, 713–723. https://doi.org/10.5194/gmd-11-713-2018

Roberts, C. D., Waters, J., Peterson, K. A., Palmer, M. D., McCarthy, G. D., Frajka-Williams, E., et al. (2013). Atmosphere drives recent interannual variability of the Atlantic meridional overturning circulation at 26.5°N. *Geophysical Research Letters*, *40*, 5164–5170. https://doi.org/10.1002/grl.50930

Robson, J., Ortega, P., & Sutton, R. (2016). A reversal of climatic trends in the North Atlantic since 2005. *Nature Geoscience*, *9*, 513–517. https://doi.org/10.1038/ngeo2727

Robson, J., Sutton, R. T., Archibald, A., Cooper, F., Christensen, M., Gray, L. J., et al. (2018). Recent multivariate changes in the North Atlantic climate system, with a focus on 2005-2016. *International Journal of Climatology*, *38*(12), 5050–5076. https://doi.org/10.1002/joc.5815

Schmitt, R. W., Bogden, P. S., & Dorman, C. E. (1989). Evaporation minus precipitation and density fluxes for the North Atlantic. *Journal of Physical Oceanography*, *19*, 1208–1221. https://doi.org/10.1175/1520-0485(1989)019<1208:empadf>2.0.co;2

Schmitz, W. J., & McCartney, M. S. (1993). On the North Atlantic circulation. *Reviews of Geophysics*, *31*, 29–49. https://doi.org/10.1029/92RG02583

Sidorenko, D., Danilov, S., Fofonova, V., Cabos, W., Koldunov, N., Scholz, P., et al. (2020). AMOC, water mass transformations and their responses to changing resolution in the Finite-volumE Sea ice–Ocean Model. *Journal of Advances in Modeling Earth Systems*, *12*, e2020MS002317. https://doi.org/10.1029/2020MS002317

Sidorenko, D., Danilov, S., Streffing, J., Fofonova, V., Goessling, H. F., Scholz, P., et al. (2021). AMOC variability and watermass transformations in the AWI climate model. *Journal of Advances in Modeling Earth Systems*, *13*, e2021MS002582. https://doi.org/10.1029/2021MS002582

Smeed, D. A., Josey, S. A., Beaulieu, C., Johns, W. E., Moat, B. I., Frajka-Williams, E., et al. (2018). The North Atlantic Ocean is in a state of reduced overturning. *Geophysical Research Letters*, *45*, 1527–1533. https://doi.org/10.1002/2017GL076350

Smith, D. M., Scaife, A. A., Eade, R., Athanasiadis, P., Bellucci, A., Bethke, I., et al. (2020). North Atlantic climate far more predictable than models imply. *Nature*, *583*, 796–800. https://doi.org/10.1038/s41586-020-2525-0

Speer, K., & Tziperman, E. (1992). Rates of water mass formation in the North Atlantic Ocean. *Journal of Physical Oceanography*, *22*, 93–104. https://doi.org/10.1175/1520-0485(1992)022<0093:rowmfi>2.0.co;2

Storkey, D., Blaker, A. T., Mathiot, P., Megann, A., Aksenov, Y., Blockley, E. W., et al. (2018). UK global ocean GO6 and GO7: A traceable hierarchy of model resolutions. *Geoscientific Model Development*, *11*, 3187–3213. https://doi.org/10.5194/gmd-11-3187-2018

Stramma, L., Kieke, D., Rhein, M., Schott, F., Yashayaev, I., & Koltermann, K. P. (2004). Deep water changes at the western boundary of the subpolar North Atlantic during 1996 to 2001. *Deep-Sea Research I*, *51*, 1033–1056. https://doi.org/10.1016/j.dsr.2004.04.001

Sun, S., & Bleck, R. (2001). Atlantic thermohaline circulation and its response to increasing CO_2 in a coupled atmosphere-ocean model. *Geophysical Research Letters*, *28*, 4223–4226. https://doi.org/10.1029/2001GL013325

Sutton, R. A., McCarthy, G. D., Robson, J., Sinha, B., Archibald, A. T., & Gray, L. J. (2018). Atlantic multidecadal variability and the U.K. ACSIS program. *Bulletin of the American Meteorological Society*, *99*(2), 415–425. https://doi.org/10.1175/BAMS-D-16-0266.1

Tsujino, H., Urakawa, S., Nakano, H., Small, R. J., Kim, W. M., Yeager, S. G., et al. (2018). JRA-55 based surface dataset for driving ocean-sea ice models (JRA55-do). *Ocean Modelling*, *130*, 79–139. https://doi.org/10.1016/j.ocemod.2018.07.002

Walin, G. (1982). On the relation between sea-surface heat flow and thermal circulation in the ocean. *Tellus*, *34*, 187–195. https://doi.org/10.3402/tellusa.v34i2.10801

Worthington, E. L., Moat, B. I., Smeed, D. A., Mecking, J. V., Marsh, R., & McCarthy, G. D. (2020). A 30-year reconstruction of the Atlantic meridional overturning circulation shows no decline. *Ocean Science*, *71*.

Worthington, L. V. (1976). On the North Atlantic circulation. *Johns Hopkins Oceanographic Studies*, *6*, 110.

Xu, X., Rhines, P. B., & Chassignet, E. P. (2018). On mapping the diapycnal water mass transformation of the upper North Atlantic Ocean. *Journal of Physical Oceanography*, *48*, 2233–2258. https://doi.org/10.1175/jpo-d-17-0223.1

Yashayaev, I., Bersch, M., & van Aken, H. M. (2007). Spreading of the Labrador Sea Water to the Irminger and Iceland basins. *Geophysical Research Letters*, *34*, L10602. https://doi.org/10.1029/2006GL028999

Zou, S., & Lozier, M. S. (2016). Breaking the linkage between Labrador Sea Water production and its export to the subtropical gyre. *Journal of Physical Oceanography*, *46*, 2169–2182. https://doi.org/10.1175/jpo-d-15-0210.1